Experimental and Computational Analysis of a R744 Flashing Ejector

Francesco Giacomelli[a], Federico Mazzelli[a]*, Krzysztof Banasiak[b], Armin Hafner[c], Adriano Milazzo[a]

[a]Department of Industrial Engineering (DIEF), University of Florence, 50139 Florence, Italy

[b]SINTEF Energy Research, 7465 Trondheim, Norway

[c]Department of Energy and Process Engineering (EPT), Norwegian University of Science and Technology,

7491 Trondheim, Norway

*federico.mazzelli@unifi.it

ABSTRACT

In this paper we present a set of experimental data acquired on a CO_2 flashing ejector designed for expansion loss recovery applications. Experimental results are compared with CFD simulations obtained using a Homogeneous Equilibrium Model (HEM) and a recently developed mixture model that treats both the liquid and vapour phases as compressible and metastable materials. The models are implemented within a commercial CFD software via user defined subroutines. Pro and cons of each of the two approaches are critically discussed in order to understand the relative performances in terms of numerical stability and accuracy. From this comparison, it can be shown that while the HEM is faster and intrinsically stable, the mixture model has the potential to better reproduce the experimental data, especially in terms of mass-flow rates predictions.

Keywords: CO2, Transcritical vapor-compression system, Expansion work recovery, CFD, look-up tables

1

Nomenclature			Greek letters		
a	Speed of sound (m s^{-1})		α	Volume fraction (-)	
e	Total specific energy (kJ kg^{-1})		β	Mass fraction of the phase (-)	
h	Specific Enthalpy (kJ kg^{-1})		Γ	Source term (kg s^{-1} m^{-3})	
$\dot{m}$	mass flow rate (kg s^{-1})		ε	Interacting portion of interface (-)	
p	Pressure (Pa)		η	Ejector efficiency (-)	
q	Heat flux (W m^{-2})		θ	Angle of diverging nozzle (°)	
s	Specific Entropy (kJ kg^{-1} K^{-1})		ρ	Density (kg m^{-3})	
T	Temperature (K)		σ	Evaporation or condensation factor (s^{-1})	
t	Time (s)		τ	Shear stress (Pa)	
u	Velocity (m s^{-1})				
x	Space coordinate (m)				
$\dot{W}$	Power (W)				
Y	Mass fraction of the species (-)				
Superscripts/subscripts			Acronyms		
c	Condensation		CFD	Computational Fluid Dynamics	
$diff$	diffuser		ER	Entrainment Ratio	
e	Evaporation		EXP	Experimental	
eff	Effective		HEM	Homogeneous Equilibrium Model	
i	Short-hand notation index		HRM	Homogeneous Relaxation Model	
in	Inlet		HVAC&R	Heating Ventilation, Air Conditioning and Refrigeration	
j	Short-hand notation index		IHE	Isentropic Homogeneous Equilibrium	
l	Liquid		MN	Motive Nozzle	
m	Mixture		SN	Suction Nozzle	
out	outlet		SST	Shear Stress Transport	
sat	Saturation		UDF	User Defined Function	
v	Vapor		UDRGM	User Defined Real Gas Model	

1. INTRODUCTION

In recent years, ejector expansion devices are emerging as enabling technology for R744 (CO_2) vapour compression cycles, which is demonstrated by increased attention manifested by academia and by leading global players in the Heating, Ventilation, Air Conditioning & Refrigeration (HVAC&R) arena [1] [2] [3] [4]. Despite this significant interest, experimental and numerical investigation of these devices are still quite far from providing a clear understanding of their complex physics. In particular, information is still lacking regarding the dynamics of nucleation, bubble growth and transport at the high speeds and typically low reduced pressures of CO_2 nozzles designed for expansion loss recovery application. At the nozzle exit, the liquid may either travel in form of droplets or create ligaments, as the liquid film is thorn away by the interaction with the surrounding turbulent vapour phase [5].

Unfortunately, the investigation of the flashing evaporation inside R744 ejectors has proved to be extremely difficult, which may be due to difficulties connected to the high-pressure and small dimensions of the flow channels.

In this field, some experimental investigation has been reported by Nakagawa et al. [6] who experimentally investigated the supersonic two-phase flow of R744 in the diverging sections of rectangular converging–diverging nozzles for inlet temperatures from 20 to 37 °C and inlet pressures from 6 to 9 MPa. They registered significant discrepancies between the measured decompression pressure profile and the one calculated according to the Isentropic Homogeneous Equilibrium (IHE) approach. Based on the results obtained, the authors advanced into the analysis of shock wave propagation in the supersonic R744 liquid–vapour flows for the same type of motive nozzle [7]. The analyses were carried out by computing shock wave pressure jumps by assuming thermodynamic equilibrium and comparing the resulting profiles with measured trends along the nozzle axis. The authors discovered that the measured two-phase shock wave pattern varied significantly from the pattern computed according to the homogeneous equilibrium shock wave approach, which indicated thermal and mechanical non-equilibrium phenomena. In addition, the authors perfomed a photographic study to visualize the evaporation onset location and to check for the presence of shocks. However, only qualitative insights on the onset location were gained and no shocks could be visually detected in the flow field.

3

More recently, Banasiak et al. [8] conducted a detailed experimental investigation into the influence of the ejector geometry on its efficiency. Multiple configurations were investigated by means of numerical simulations and experimental work. Results of these analyses indicated that the ejector efficiency is notably dependent on the mixing section length and diameter, as well as on the diffuser divergence angle. Finally, Zhu et al. [9] attempted a flow visualization study of the mixing chamber of a CO_2 flashing ejector. Unfortunately, the authors reported severe difficulties in implementing a Schlieren visualization method. Therefore, the investigations were limited to the analysis of the motive jet expansion angle in the mixing chamber via direct photography method.

Due to the difficulties inherent in the experimental investigation, Computational Fluid Dynamics (CFD) analyses become crucial for the understanding of the internal flow dynamics. To date, CFD studies on flashing flows are mostly focused on the analysis of water, due to its role in the safety of nuclear reactors or industrial processes involving pressurized pipelines. The literature in this field is quite vast and review works are reported by [10] [11] [12]. To a less extent, the numerical study of flashing CO_2 have also been carried out in the last decade. Table 1 summarizes the various approaches that were investigated in the literature regarding the CFD simulation of CO_2 flashing nozzles and ejectors.

Lucas et al. [13] used a Homogeneous Equilibrium Model (HEM) to simulate the flashing flow of CO_2 within ejectors (for a description of different modelling strategies such as HEM or HRM, the reader may refer to [14]). The model was implemented within the open source CFD code Open-FOAM [15]. The numerical model predicted the motive flow rate within an error of 10%. In addition, the ejector pressure recovery was calculated with an average discrepancy of 10% and 20% when the ejector is operated without and with a suction flow, respectively (the suction flow rate is prescribed as a boundary condition). Smolka et al. [16] employed a HEM based on a modified enthalpy transport equation implemented in the commercial code ANSYS Fluent [17]. The authors performed a fully 3D simulations with tangential suction flow inlet. The results of the model showed average discrepancies for the primary and secondary flow of 5.6% and 10.1%, respectively. In addition, the pressure lift distribution was well reproduced. A modelling approach similar to that of Smolka et al. [16] was used by Giacomelli et al. in [18] who simulated and experimentally tested a CO_2 flashing ejector under both supercritical and subcritical motive inlet conditions. The fluid properties were evaluated through lookup-tables interpolation generated from NIST Refprop libraries [19]. The result of the study revealed that

4

the motive flow rate is reproduced with an error between 12% and 19%. However, the discrepancy on the secondary flow rate is significantly higher (around 20-30% with peaks that can reach up to 50%). The larger discrepancies were mostly seen when the mixing chamber was in choked conditions. These errors, may arise from a wrong estimation of the mass flow rate and void fraction of the primary flow due to the HEM modelling assumption, or from neglecting the swirl velocity component at the suction inlet.

In 2010, Angielczyk et al. [20] carried out a 1D simulation of the nozzle investigated by Nakagawa et al. [6] by using a Homogeneous Relaxation Model (HRM) with a relaxation time calibrated against the experiments. The model compared favorably with the experimental pressure trends. However, the authors reported that information on temperature, quality and critical flow rate would be required to define a suitable correlation for the relaxation time. More recently, Haida et al. [21] have implemented a HRM in ANSYS Fluent. Three different formulation of the HRM relaxation times were confronted with an HEM scheme, including a modified HRM formulation calibrated by means of genetic algorithms. The simulations were compared against experimental data on motive and suction mass flow rates, which resulted in variable discrepancies that ranged from 5% to 50%, with lower values for the motive mass flow rates and for the transcritical operating regime. Interestingly, in the transcritical conditions the HRM and HEM performance were similar, probably due to the small relaxation time characteristic of the flashing evaporation near the critical point.

In 2012, Yazdani et al. [22] employed a "Mixture-Model" approach using the commercial code ANSYS Fluent. For the phase change model, the authors combined a thermally-controlled boiling model with an inertia-controlled cavitation model. The simulations revealed that the phase change is dominated by boiling near the nozzle centerline and by cavitation near the walls. The model predicted ejector pressure rise and entrainment ratio to within 10% of experimental data (however, it should be noted that modelling the flashing of CO_2 as the superposition of boiling and cavitation may be quite difficult to justify from a thermodynamic point of view, as these two phenomena cannot be considered independent, see for instance [10]).

Finally, Giacomelli et al. [23] developed a mixture model approach that treats both the liquid and vapour phases as compressible materials. The properties of each phase were obtained via look-up tables that extend in the whole domain of interest, including supercritical and metastable regions. The method was implemented within the commercial CFD software ANSYS Fluent and tested against the flashing R744 nozzle test-case of Nakagawa et al. [6]. The results showed that both pressure and temperature profiles are qualitatively well

reproduced by the model. The maximum discrepancy with experiments was found for Case 1, in which the relative errors for pressure and temperature were respectively 34% and 6.5%. However, no validation could be made in terms of mass flow rate because no measurement were reported by [6].

In this respect, one of the major problems that hinders the development of more accurate CFD model is the lack of reliable and detailed experimental test campaigns. Consequently, one of the main goal of this paper is to present a new set of experimental data that can be used for validation of both CFD and thermodynamic models. Therefore, a great care was devoted to control the dimensional accuracy of the various ejector parts during the manufacturing process. Moreover, detailed calculations were performed in order to achieve a reliable estimation of the measurement uncertainty. Finally, the obtained experimental results were compared with the newly developed CFD model described in [23] in order to gain more insights of the ejector internal flow behaviour. Differences between the Mixture Model and the HEM described in [18] are also analyzed in the paper.

6

| Authors	Test Case	Software	Numerical Setup	Multiphase Approach	Fluid Properties Description	Results and Remarks
Lucas et al. [13]	Ejector	OpenFOAM	- Pressure based solver - Second Order Accuracy - 2D axisymmetric - Structured Grid - 116 000 cells	HEM	Fluid Properties from TEMO-media Library invoked at runtime	- the model predicts the motive mass flow rate within an error margin of 10% (A/N: the suction flow rate is prescribed as a boundary condition) - The pressure recovery of the ejector operated without a suction flow is determined with an error of 10%. This error increases to 20% when the ejector is operated with a suction flow
Smolka et al. [16]	Ejector	ANSYS Fluent	- Pressure based solver - Second Order Accuracy - 3D with tangent suction inlet - Hybrid Grid - 170 000 or 360 000 cells	HEM	Fluid Properties from NIST Refprop	- The average discrepancies for the primary and secondary flow are 5.6% and 10.1%, respectively. - The pressure lift distribution is very well reproduced. - The 3D geometry showed non-symmetrical features in the results
Giacomelli et al. [18]	Ejector	ANSYS Fluent	- Pressure based coupled solver - Second Order Accuracy - 2D axisymmetric - Structured Grid - 50 000 cells	HEM	Lookup Tables generated from NIST Refprop	- The primary nozzle flow rate is reproduced with a relative error between 12% and 19% - The discrepancy on the secondary flow rate is around 20-30% with peaks that can reach up to 50% - Larger discrepancies are seen when the mixing chamber is predicted to be in choked conditions. - Neglecting the suction swirl velocity component has also an impact on suction flow calculations
Angielczyk et al. [20]	Nozzle	OpenFOAM	- 1D domain - Direct integration of the differential equation system	HRM	Metastable liquid phase calculated via 3 order spline extrapolation of isochors	- The model compares favourably with the experimental pressure trends. - Information on temperature, quality and critical flow rate are deemed to be required to define a suitable correlation for the relaxation time.
Haida et al. [21]	Ejector	ANSYS Fluent	- Pressure based coupled solver - Second Order Accuracy - 2D axisymmetric - Structured Grid - 10 000 cells	HRM	Fluid properties from NIST Refprop	- Various formulation of HRM relaxation times and one HEM schemes are confronted. - Simulations are compared against experimental data on motive and suction mass flow rates. - Discrepancies are highly variable and range from 5% to 50%, with lower values for the motive mass flow rates and for the transcritical operating regime (where HRM and HEM have similar accuracies).
Yazdani et al. [22]	Ejector	ANSYS Fluent	- Segregated Pressure based solver - Second Order Accuracy - 2D axisymmetric - Structured Grid - 80 000 cells	Mixture with boiling and cavitation phase change models	1. Supercritical fluid, subcooled liquid and saturated regions: interpolation from REFPROP 2. Superheated vapour: Peng–Robinson EOS	- Simulations revealed that phase change is dominated by boiling near the nozzle centreline and by cavitation near the walls. - The model predicted ejector pressure rise and entrainment ratio to within 10% of experimental data
Giacomelli et al. [23]	Nozzle	ANSYS Fluent	- Coupled Pressure based solver - Third Order Accuracy - 2D planar symmetry - Structured Grid - 12 000 cells	Mixture with Lee evaporation model	Lookup Tables generated from NIST Refprop Both Phases treated as compressible and Metastable	- Both pressure and temperature profiles are qualitatively well reproduced by the model. - The maximum discrepancies for pressure and temperature were respectively 34% and 6.5%. - Validation could not be made in terms of mass flow rate because no experimental data were reported

Table 1 – Summary of CFD approaches for the simulation of CO_2 flashing flows

2. EXPERIMENTAL ANALYSIS

2.1 Experimental setup

The experimental tests considered for this research were conducted at the Norwegian University of Science and Technology and SINTEF Energy laboratories (Norway).

The test-rig configuration is shown in Figure 1. Heat input and output are provided for the system via two separate glycol loops at the evaporator (blue) and the gas cooler (red), while additional heat is provided at the air heat exchanger (green) in order to achieve a higher pressure lift of the ejector. The measurement system is based on T-type thermocouples, absolute and differential pressure sensors (piezoelectric elements), and Coriolis-type mass flow meters. The gauge pressure transmitters were connected by 1/8" stainless steel tubing to the pressure measurement ports (0.5 mm diameter) drilled perpendicularly to the flow direction in the ejector block. Detailed information on the measurement apparatus are provided in Table 2. The uncertainties for all the measured quantities are evaluated considering both instrument and random errors as described in [18]. The mean values of the uncertainties were found to be $\pm 0.3\ K$ for temperatures, $\pm 15000\ Pa$ for pressures and $\pm 0.005\ kg\ s^{-1}$ for mass flow rates.
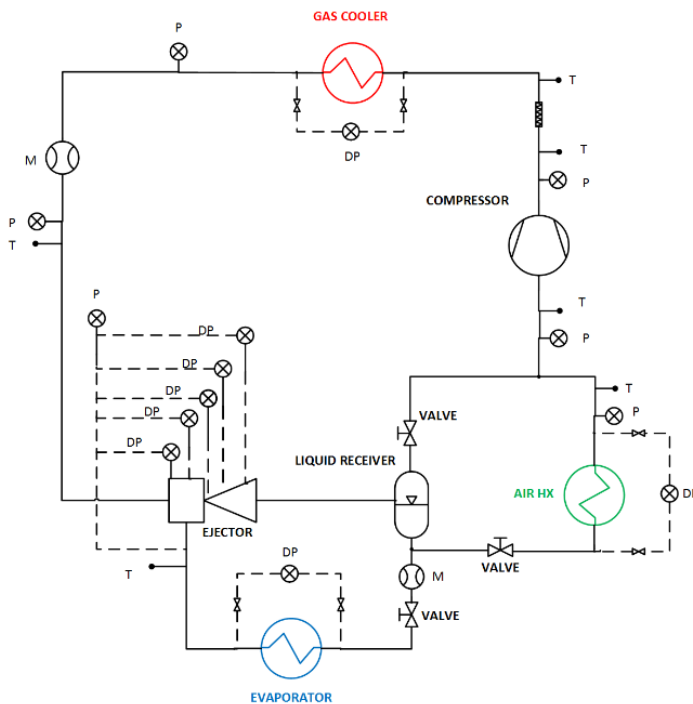
Compressor	piston-type, two-cylinder DORIN CD38OH
Compressor inverter	TOSHIBA VF-S7
Gas cooler	plate heat exchanger, CO_2-to-glycol KAORI K040C-20C
Evaporator	plate heat exchanger, glycol-to-CO_2 KAORI K040C-12C
Liquid separator	prototype 1L tank by OBRIST Engineering
Glycol pumps	centrifugal GRUNDFOS CHI 2-50 A-W-G-BQQV
Glycol pumps inverters	inverters TOSHIBA VF-S11
Electric heater	BACKER 10 kW

8

Figure 1 - Experimental test-rig layout. T: T-type thermocouple; P: pressure sensor; DP: differential pressure sensor; M: Coriolis mass-flow meter
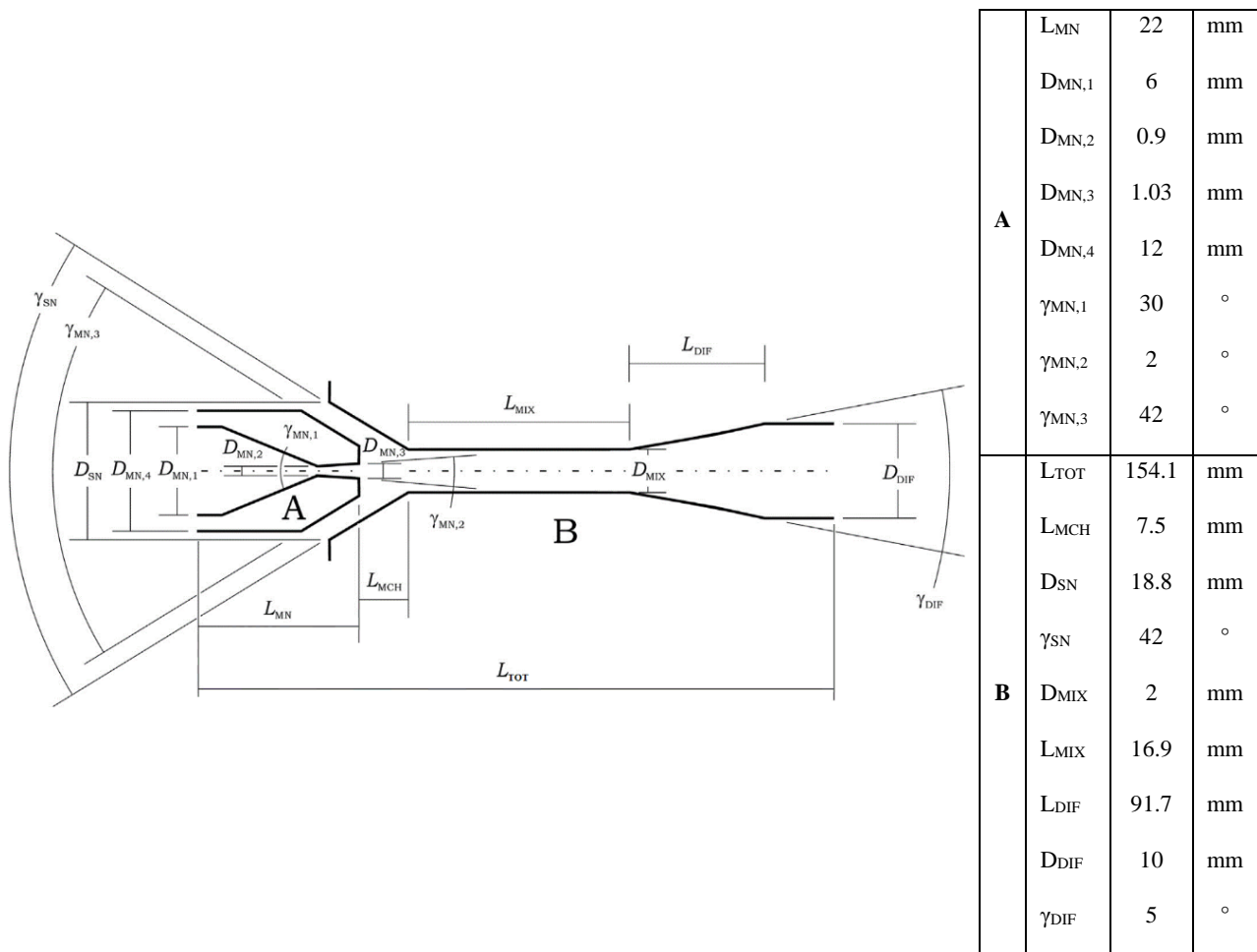
Measured quantity	Instrument	calibration range	accuracy
High pressure transducer	*Endress and Hauser Cerabar S PMP71*	*70–140 bar*	*±0.15% of range*
Low pressure transducer	*Endress and Hauser Cerabar S PMP71*	*10-70 bar*	*±0.15% of range*
Differential pressure transmitters	*Endress and Hauser Deltabar S PMD75*	*span 0–15 bar*	*±0.075% of range*
Suction stream mass flow meter	*Rheonik RHE08 RHM04*	*0.2–10 kg min⁻¹*	*±0.2% measured value*
Motive stream mass flow meter	*Rheonik RHE08 RHM06*	*0.5–20 kg min⁻¹*	*±0.2% measured value*
Temperature measurement	*Thermocouples Cu-CuNi Omega TMTSS*	*-200–350 °C*	*±0.75% measured value*

Table 2 – Measurement apparatus

The main dimensions of the ejector are shown in Figure 2. The motive nozzle throat diameter was sized to produce a flow rate that matches the power requirement of a small-capacity transcritical heat pump. The rest of the body (mixing chamber and diffuser) was designed to reach the pressure lift and mass entrainment ratio (eq. (2) and (3) in section 2.2) for typical operating conditions of heat pump applications: P_{MN}= 90 bar, T_{MN}=35 °C, P_{SN} = 35 bar. It should be noted that in the present configuration the suction flow enters the ejector with a tangential velocity component. This effect was obtained by designing the secondary inlet port with an angle of 62.5° with respect to the radial direction (where 0° is considered fully radial entrance and 90° is fully tangential). The swirl of the suction has the effect of increasing the ejector entrainment ratio and must be considered in computational analysis.

The surface roughness of the internal walls was taken into consideration during the ejector design and manufacturing in order to achieve Rz 1 for all the internal channels. The surface quality was inspected after

9

the manufacturing process by an external company who certified the achievement of the design value. More details on the ejector geometry can be found in [24].

A	L_{MN}	22	mm
	$D_{MN,1}$	6	mm
	$D_{MN,2}$	0.9	mm
	$D_{MN,3}$	1.03	mm
	$D_{MN,4}$	12	mm
	$\gamma_{MN,1}$	30	°
	$\gamma_{MN,2}$	2	°
	$\gamma_{MN,3}$	42	°
B	L_{TOT}	154.1	mm
	L_{MCH}	7.5	mm
	D_{SN}	18.8	mm
	γ_{SN}	42	°
	D_{MIX}	2	mm
	L_{MIX}	16.9	mm
	L_{DIF}	91.7	mm
	D_{DIF}	10	mm
	γ_{DIF}	5	°

Figure 2 - Basic dimensions of the ejector (image not to scale). "A" refers to the motive nozzle geometry while "B" corresponds to the suction entry channel, mixing section and diffuser. MN and SN stand for Motive Nozzle and Suction Nozzle, respectively

2.2 Experimental dataset

All the motive and suction inlet conditions examined during the test campaign are shown in the P-h diagram of Figure 3. Table 3 and Table 4 summarize the boundary conditions and mass flow rate data of the most of these tests along with their calculated uncertainties. The curves are obtained by keeping approximately constant the motive inlet conditions while varying the suction pressure. A total of nine curves are obtained, with motive inlet states that range from supercritical to subcooled liquid regions. In this respect, multiple tests were done in the region where the CO_2 temperature and pressure are respectively below and above the corresponding critical values. For this region, the authors are not aware of a commonly agreed name, which is sometimes

10

referred to as compressed liquid region or compressible liquid. Consequently, in Table 4 and throughout the text we generally refer to "subcritical condition" for motive inlet states with temperatures below the critical values, whereas the term "subcooled liquid" was used to specifically refer to conditions with both subcritical temperatures and pressures.

The nine experimental curves are plotted in Figure 4 as a function of the of the ejector pressure lift and efficiency, defined here following the work of Elbel and Hrnjak [25]:

$$\eta = \frac{\dot{W}_{rec}}{\dot{W}_{rec\_max}} = ER \frac{h(P_{diff,out}; S_{SN,in}) - h_{SN,in}}{h_{MN,in} - h(P_{diff,out}; S_{MN,in})} \qquad (1)$$

$$ER = \frac{\dot{m}_{SN}}{\dot{m}_{MN}} \qquad (2)$$

$$P_{lift} = P_{diff,OUT} - P_{SN} \qquad (3)$$

where $\dot{W}_{rec}$ representes the expansion work recovered and used to compress the suction stream and $\dot{W}_{rec\_max}$ is the maximum recoverable work from motive stream.

As can be seen, the ejector efficiency presents a maximum at a value of pressure lift close to 9. This is particularly evident in supercritical conditions. Such maximum is not reached for subcritical conditions due to the fact that the system could not maintain stable operating regime at high values of pressure lift and low motive inlet pressures and temperatures.

The maximum of Figure 4 can be explained in terms of a trade-off between entrainment ratio and pressure lift. Indeed, the recovered energy from the motive stream can be either used to entrain a greater quantity of suction flow or to compress the same stream at higher pressures. This trade-off is clearly visible in Figure 5 that plots the levels of ejector efficiency as a function of the pressure lift and entrainment ratio. As can be seen, the cases with higher efficiency tends to concentrate toward the centre of the diagram (high ER and lift), while the efficiency is lower towards the right and left extremities.

Among all the experimental tests, two curves have been chosen for comparison with CFD, shown in Figure 6. The two set of data share the same motive inlet pressure but possess different motive inlet temperatures. This choice was specifically made to analyse the differences between supercritical and subcritical motive inlet

conditions. Moreover, different suction pressures were simulated in order to verify the capability of the CFD

model to correctly reproduce the mixing and entrainment process with a varying pressure lift.
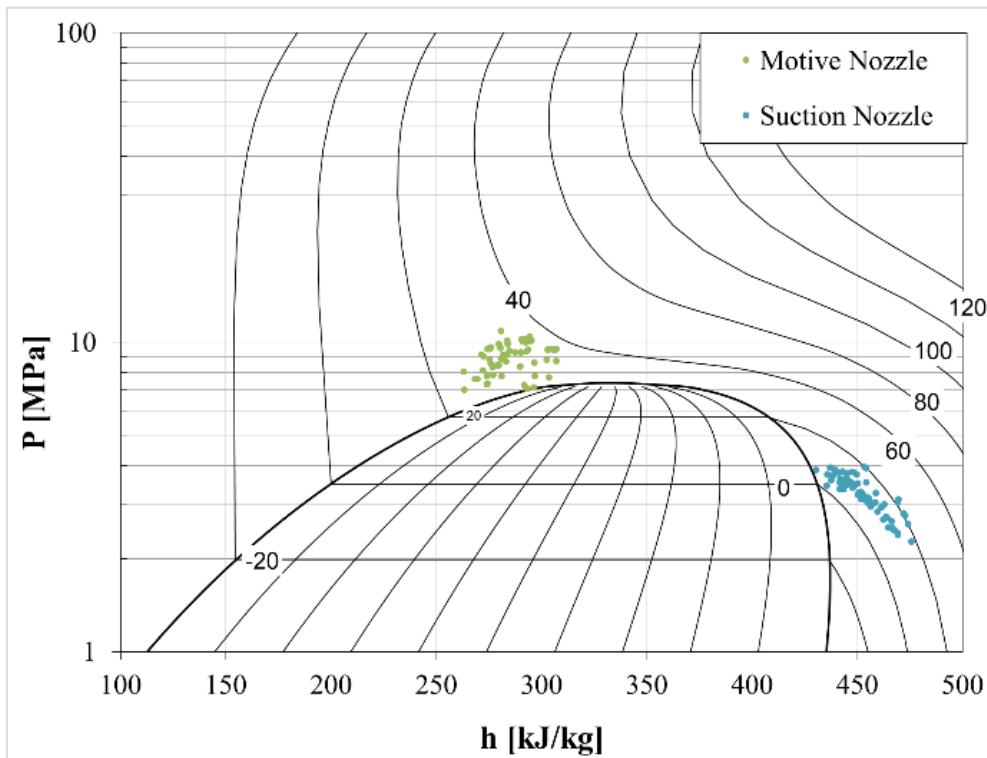

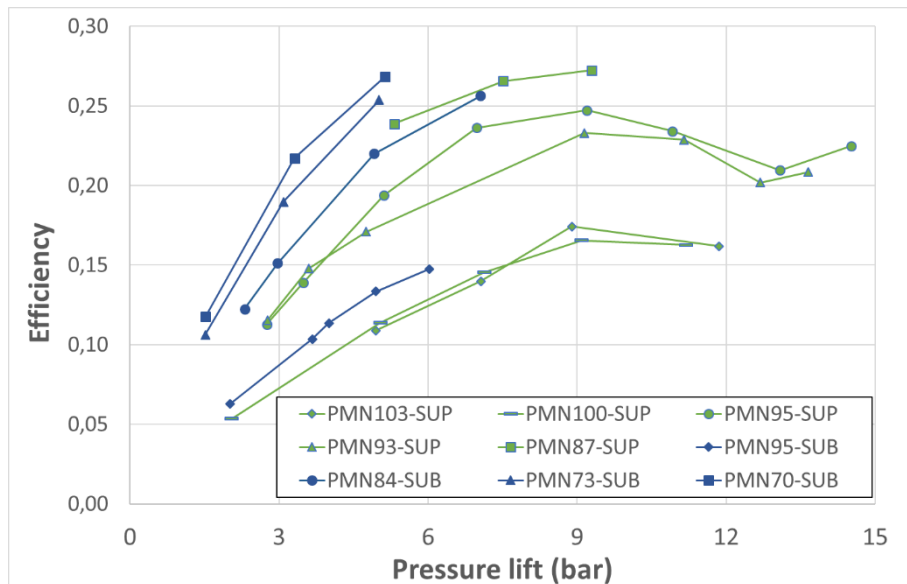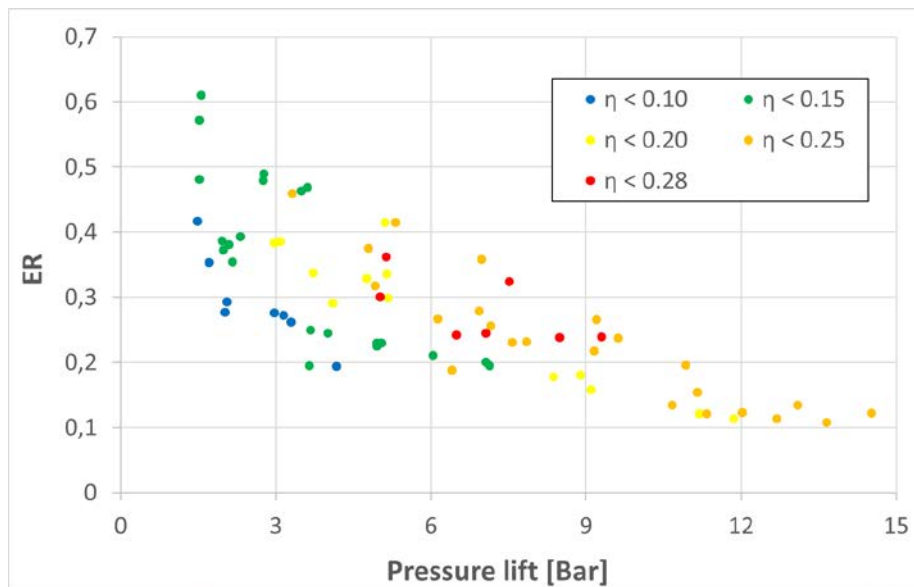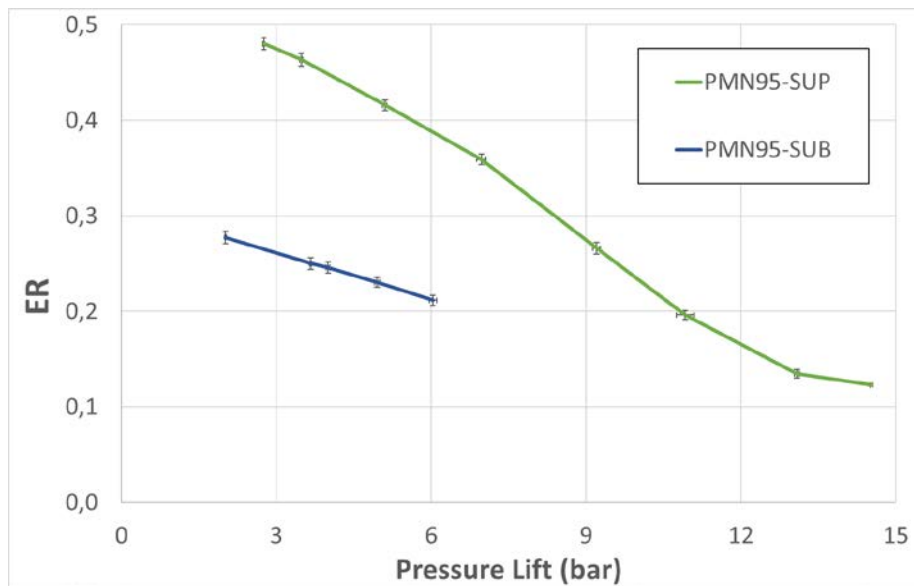**Figure 3 - P-h diagram of experimental inlet conditions**

Figure 4 - Ejector efficiency versus pressure lift

12

Figure 5 – Performance parameters plot

Figure 6 – Experimental curves selected for comparison with CFD

Curve	Case	MN Inlet conditions	P_{MN} [bar]	T_{MN} [°C]	M_{MN} [kg min^{-1}]	P_{SN} [bar]	T_{SN} [°C]	M_{SN} [kg min^{-1}]	P_{EJ1} [bar]	P_{EJ2} [bar]	P_{EJ3} [bar]	P_{EJ4} [bar]	P_{EJ5} [bar]	ER [-]
PMN103-SUP	1	supercritical	104,1±1,9	36,9±1,3	2,865±0,022	30,83±0,23	10,5±0,3	0,576±0,005	30,78±0,26	29,92±0,33	23,57±0,74	37,78±0,47	37,89±0,47	0,201±0,003
	2	supercritical	102,6±1,4	36,6±1	2,799±0,021	24,87±0,17	12,6±0,7	0,32±0,014	24,85±0,21	26,69±0,27	29,17±0,42	36,64±0,38	36,72±0,38	0,114±0,006
	3	supercritical	102,5±1,7	36,4±1,2	2,619±0,039	28,4±0,22	10,8±0,3	0,475±0,008	28,34±0,28	28,4±0,31	26,29±0,54	37,17±0,43	37,29±0,43	0,181±0,006
	4	supercritical	101,9±1,6	35,5±1,2	2,877±0,022	32,76±0,2	9,7±0,3	0,649±0,011	32,69±0,25	31,19±0,29	20,89±0,5	37,61±0,35	37,71±0,35	0,226±0,006
PMN100-SUP	5	supercritical	101,2±0,6	36,6±0,5	2,723±0,01	24,65±0,1	13±0,8	0,331±0,009	24,62±0,14	26,35±0,15	28,24±0,23	35,76±0,2	35,84±0,2	0,122±0,004
	6	supercritical	100,9±0,2	35,8±0,3	2,786±0,007	32,13±0,08	10,2±0,3	0,642±0,01	32,09±0,08	30,57±0,12	21,43±0,19	37,06±0,12	37,16±0,12	0,231±0,004
	7	supercritical	100,3±0,4	35,9±0,3	2,741±0,016	29,45±0,24	9,6±2,9	0,535±0,01	29,4±0,27	28,87±0,32	24,86±0,61	36,46±0,4	36,57±0,4	0,195±0,005
	8	supercritical	100,3±0,5	36,2±0,4	2,718±0,009	34,78±0,08	10±0,3	0,799±0,012	34,74±0,1	32,22±0,12	20,44±0,13	36,73±0,13	36,83±0,13	0,294±0,005
	9	supercritical	100,1±0,4	35,8±0,4	2,738±0,012	27,1±0,19	13±1,4	0,434±0,012	27,06±0,23	27,48±0,26	26,31±0,44	36,07±0,33	36,19±0,34	0,158±0,005
PMN95-SUP	10	supercritical	95,3±0,1	37,3±0,3	2,273±0,006	37,9±0,06	10±0,3	1,053±0,013	37,83±0,07	32,98±0,08	30,99±0,12	41,25±0,09	41,38±0,09	0,463±0,007
	11	supercritical	95,2±0,2	37,7±0,3	2,215±0,01	29,29±0,25	13,6±2,4	0,434±0,009	29,26±0,27	29,33±0,35	35,57±0,45	40,14±0,42	40,21±0,42	0,196±0,005
	12	supercritical	95±0,1	37,5±0,3	2,234±0,007	33,82±0,14	9±1,7	0,802±0,01	33,76±0,15	31,32±0,22	33,28±0,3	40,7±0,23	40,79±0,23	0,359±0,006
	13	supercritical	94,9±0,1	37,2±0,3	2,256±0,006	35,94±0,06	10,2±0,3	0,938±0,01	35,88±0,07	31,99±0,1	32,21±0,12	40,92±0,1	41,05±0,11	0,416±0,005
	14	supercritical	94,8±0,1	36,9±0,3	2,277±0,006	38,59±0,06	9,7±0,3	1,093±0,012	38,51±0,06	33,42±0,08	30,33±0,1	41,22±0,07	41,34±0,08	0,48±0,006
	15	supercritical	94,8±0,1	37,4±0,3	2,217±0,005	24,17±0,06	13,8±0,3	0,273±0,002	24,15±0,07	27,22±0,07	35,62±0,09	38,64±0,08	38,69±0,08	0,123±0,001
	16	supercritical	94,7±0,1	37,5±0,3	2,201±0,006	26,43±0,09	13,9±1	0,297±0,009	26,41±0,11	27,76±0,14	35,62±0,17	39,46±0,14	39,51±0,14	0,135±0,004
	17	supercritical	94,7±0,2	37,4±0,3	2,212±0,013	31,14±0,24	8,3±5,1	0,589±0,01	31,1±0,25	30,2±0,33	34,66±0,45	40,26±0,31	40,34±0,31	0,266±0,006
PMN93-SUP	18	supercritical	94,7±0,1	36,9±0,3	2,275±0,006	38,62±0,06	9,9±0,3	1,068±0,011	38,55±0,07	33,93±0,07	32,59±0,1	42,11±0,07	42,22±0,08	0,47±0,006
	19	supercritical	94,7±0,1	36,9±0,3	2,275±0,006	39,39±0,05	9,6±0,3	1,115±0,009	39,34±0,07	34,2±0,07	31,77±0,09	42,05±0,07	42,16±0,07	0,49±0,005
	20	supercritical	94,5±0,2	34,9±0,3	2,461±0,01	30,13±0,22	11,5±1,9	0,536±0,008	30,1±0,22	29,41±0,32	32,54±0,47	39,2±0,37	39,28±0,37	0,218±0,004
	21	supercritical	93,5±0,1	34,6±0,3	2,421±0,008	23,9±0,06	13,3±0,3	0,263±0,007	23,89±0,08	27,04±0,11	33,84±0,11	37,49±0,1	37,54±0,1	0,109±0,003
	22	supercritical	92,8±0,1	33,9±0,3	2,454±0,007	27,34±0,1	12,9±0,9	0,38±0,013	27,32±0,11	27,98±0,14	32,83±0,2	38,41±0,17	38,49±0,17	0,155±0,006
	23	supercritical	92,7±0,1	33,8±0,3	2,452±0,007	25,21±0,09	12,7±0,4	0,279±0,01	25,2±0,1	27,11±0,15	33,52±0,19	37,84±0,14	37,9±0,14	0,114±0,004
	24	supercritical	92,7±0,6	33,2±0,5	2,539±0,008	35,27±0,08	10,3±0,3	0,836±0,009	35,21±0,08	31,78±0,12	29,3±0,22	39,92±0,15	40,02±0,15	0,329±0,005
PMN87-SUP	25	supercritical	87,6±0,3	35±0,4	1,933±0,009	32,19±0,12	8,6±1,2	0,628±0,009	32,16±0,14	30,77±0,16	35,16±0,18	39,64±0,18	39,7±0,18	0,325±0,006
	26	supercritical	87,2±0,4	35,5±0,4	1,848±0,01	31,13±0,17	22,2±0,5	0,443±0,006	31,11±0,17	30,67±0,21	37,19±0,27	40,37±0,23	40,43±0,23	0,24±0,005
	27	supercritical	85,9±0,7	33,6±0,7	1,961±0,011	34,23±0,21	6,9±4,2	0,814±0,014	34,18±0,24	31,38±0,35	33,95±0,42	39,45±0,39	39,55±0,39	0,415±0,01

Table 3 - Tested Case Boundary Conditions for supercritical motive nozzle inlet. MN = Motive Nozzle; SN = Suction Nozzle; OUT = Outlet

14

Curve	Case	MN Inlet conditions	PMN [bar]	TMN [°C]	MMN [kg/min]	PSN [bar]	TSN [°C]	MSN [kg/min]	P_EJ1 [bar]	P_EJ2 [bar]	P_EJ3 [bar]	P_EJ4 [bar]	P_EJ5 [bar]	ER [-]
PMN95-SUB	28	Subcritical	96,3±0,5	30,8±0,5	3,011±0,014	33,57±0,11	5,8±0,5	0,637±0,014	33,5±0,17	32,09±0,2	27,49±0,38	39,5±0,18	39,6±0,18	0,211±0,006
	29	Subcritical	95,3±0,4	30,4±0,4	2,996±0,009	34,65±0,07	8,2±0,3	0,69±0,013	34,54±0,11	32,72±0,11	26,08±0,21	39,48±0,11	39,6±0,12	0,23±0,005
	30	Subcritical	95,3±0,1	30,4±0,3	2,997±0,011	35,98±0,06	8,5±0,3	0,75±0,015	35,9±0,08	33,64±0,08	23,78±0,14	39,55±0,08	39,65±0,08	0,25±0,006
	31	Subcritical	95,1±0,2	30,2±0,3	3,001±0,008	37,77±0,06	12,3±0,3	0,833±0,017	37,74±0,07	34,93±0,09	22,39±0,07	39,7±0,07	39,78±0,08	0,278±0,007
	32	Subcritical	94,9±0,3	30,4±0,3	2,97±0,009	35,5±0,06	9,4±0,3	0,73±0,015	35,4±0,09	33,22±0,08	24,5±0,15	39,38±0,09	39,5±0,09	0,246±0,006
PMN84-SUB	33	Subcritical	84,2±1	29,9±0,9	2,3±0,017	32,57±0,27	15,4±0,3	0,564±0,013	32,53±0,28	31,34±0,33	34,36±0,6	39,55±0,47	39,63±0,48	0,245±0,007
	34	Subcritical	84,1±0,6	29,7±0,7	2,328±0,016	37,39±0,23	14,8±0,4	0,894±0,014	37,33±0,24	33,19±0,33	32,52±0,63	40,25±0,31	40,36±0,31	0,384±0,009
	35	Subcritical	84,1±0,7	29,7±0,8	2,323±0,018	35,2±0,25	15,2±0,3	0,739±0,011	35,15±0,26	32,41±0,32	33,38±0,61	40,03±0,38	40,12±0,38	0,318±0,007
	36	Subcritical	83,2±0,5	29±0,6	2,353±0,016	38,02±0,18	14,5±0,3	0,927±0,014	37,96±0,19	33,51±0,28	32,07±0,56	40,22±0,23	40,33±0,23	0,394±0,009
PMN73-SUB	37	Subcooled liquid	73,6±0,1	26,8±0,3	1,867±0,006	34,79±0,09	6,7±2,3	0,899±0,016	34,72±0,11	30,9±0,21	30,39±0,14	36,22±0,11	36,31±0,11	0,481±0,01
	38	Subcooled liquid	73,4±0,1	26,7±0,3	1,862±0,007	32,86±0,09	10,6±0,9	0,72±0,011	32,8±0,1	29,91±0,11	31,05±0,14	35,87±0,12	35,95±0,12	0,387±0,007
	39	Subcooled liquid	72,9±0,2	26,6±0,3	1,83±0,014	30,28±0,24	9,5±5,3	0,552±0,008	30,23±0,27	28,85±0,3	31,17±0,36	35,22±0,33	35,29±0,33	0,302±0,007
PMN70-SUB	40	Subcooled liquid	71,6±0,4	29,4±0,4	1,483±0,012	25,89±0,11	20±2,6	0,537±0,004	25,84±0,15	24,01±0,15	27,49±0,16	30,93±0,17	31,02±0,17	0,363±0,006
	41	Subcooled liquid	70,9±0,5	29±0,4	1,495±0,015	30,35±0,14	21±4,6	0,855±0,01	30,27±0,17	25,55±0,23	26,21±0,22	31,78±0,18	31,87±0,17	0,572±0,013
	42	Subcooled liquid	70,9±0,4	28,9±0,4	1,488±0,011	28,02±0,1	20,6±3,4	0,685±0,007	27,96±0,13	24,54±0,15	26,79±0,14	31,27±0,15	31,33±0,15	0,46±0,008

Table 4 - Tested Case Boundary Conditions for subcritical motive nozzle inlet. MN = Motive Nozzle; SN = Suction Nozzle; OUT = Outlet

3. NUMERICAL ANALYSIS

3.1 Mathematical model

The numerical model presented in this section was implemented within the CFD package ANSYS Fluent v19.0 [17]. The method is based on a Mixture-Model approach and is described in detail by Giacomelli et al. [23]. The set of averaged conservation equations for mass, momentum and energy has the following form:

$$\frac{\partial \rho_m}{\partial t} + \frac{\partial \rho_m u_{mj}}{\partial x_j} = 0$$

$$\frac{\partial \rho_m u_{mi}}{\partial t} + \frac{\partial \rho_m u_{mi} u_{mj}}{\partial x_j} = -\frac{\partial p}{\partial x_j} + \frac{\partial \tau_{ij\_eff}}{\partial x_j}$$

$$\frac{\partial \rho_m e_m}{\partial t} + \frac{\partial \rho_m u_{mj} h_m}{\partial x_j} = \frac{\partial q_{j\_eff}}{\partial x_j} + \frac{\partial u_{mi} \tau_{ij\_eff}}{\partial x_j} \tag{4}$$

$$\frac{\partial \rho_v \alpha_v}{\partial t} + \frac{\partial \rho_v u_{mj} \alpha_v}{\partial x_j} = \Gamma_e - \Gamma_c$$

The last equation of (4) is complemented with the following constraint:

$$\alpha_v + \alpha_l = 1 \tag{5}$$

Where p, ρ_m, u_m and h_m are the mixture pressure, density, velocity and specific enthalpy; q_{j_eff} and τ_{ij_eff} are the effective (molecular plus turbulent) heat and momentum flux; ρ_v and α_v are the vapor density and volume fraction.

Γ_e and Γ_c in the last equation of (4) are the source terms related to the evaporation and condensation process respectively. The equation for these two terms are obtained from the Hertz-Knudsen theory (see [17] or [26]) and can be written in the following form:

$$\Gamma_e = \sigma_e \alpha_l \rho_l \frac{T - T_{sat}}{T_{sat}} \tag{6}$$

16

$$\Gamma_c = \sigma_c \alpha_v \rho_v \frac{T_{sat} - T}{T_{sat}} \tag{7}$$

Where the first of the two equation is valid if $T > T_{sat}$, whereas the second holds if $T < T_{sat}$; σ_e and σ_c are the evaporation and condensation factor and can be considered as the inverse of a relaxation time.

In the present mixture approach, the phases are assumed to share the same pressure and temperature and the effect of slip velocity between the phases has been neglected. The turbulence model adopted for all the simulations is the 2-equations *k-ω SST* model [17].

Moreover, since the flow is expected to be transonic, the definition of the two-phase sound speed requires special consideration. As shown in [27], the following equation was found to be used by the ANSYS Fluent solver:

$$a = \sqrt{\frac{1}{(\alpha_l \rho_l + \alpha_v \rho_v)\left(\frac{\alpha_l}{\rho_l a_l^2} + \frac{\alpha_v}{\rho_v a_v^2}\right)}} \tag{8}$$

This equation represents the harmonic-average of the sound speeds of saturated phases [28] [29] and is commonly used in CFD simulation of water and steam mixtures [30]. A deeper discussion about the sound speed formulation is provided in section 4 of this paper.

Equations from (4) to (7) form a system that must be complemented with the thermodynamic and transport properties of the refrigerant. In the present approach, both the liquid and vapour phase are treated as compressible materials, which means that all thermodynamic properties vary with temperature and pressure.

To the best of the authors' knowledge, the only way to achieve this in Fluent is by using a Multispecies *User-Defined Real Gas Model* (m-UDRGM) (see [23] for a detailed explanation).

This procedure allows definition of two different *species* and two different *phases*, as illustrated in Figure 7.

In total, four *species* are activated, two of which must be considered "dummy". In order to do this, the mass transfer mechanisms must be activated only for the two active *species*. Moreover, the <u>mass</u> fraction Y of the dummy species at the ejector boundaries must be set to a constant zero value in order to avoid dummy species from entering the computational domain. Finally, unphysical diffusion between the active species is suppressed by setting the molecular diffusivity of each material to a nearly-zero value and by imposing a very large

17

turbulent Schmidt number (it should be noted that physically only one species exists inside the ejector, i.e., CO_2; therefore, any molecular diffusion between the active "liquid species" and "vapour species" must be suppressed in the solver settings). As a result, the final set of equations corresponds to the Mixture-Model equations described in the previous section.
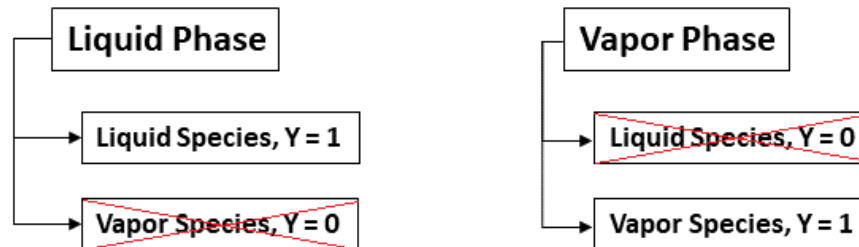

Figure 7 - multispecies multiphase model layout (the "dummy" species are crossed in red)

3.2 Numerical setup

Figure 8 shows the computational domain used for the simulations, which consists of a 2D axis-symmetrical section of the ejector. The swirled flow at the suction inlet has been modelled by solving an additional transport equation for angular momentum.

The solver uses a coupled pressure-based approach, which is the only option available in the Fluent multiphase solver framework. However, although it is generally acknowledged that density-based solvers perform better in highly compressible flows, pressure-based schemes have also been successfully applied for the simulations of multiphase compressible flows with discontinuities (e.g. [30]).

A second order accurate up-wind scheme is selected for the spatial discretization of all transport equations except for the volume fraction and momentum ones. The first of these is discretized by means of a 3rd order QUICK scheme, whereas, for the latter, a power-law scheme had to be chosen, due to numerical instabilities connected with the pressure-velocity coupling.

The properties of both phases are obtained from the NIST Refprop libraries [19], which use the Span and Wagner equation of state [31]. The properties are inserted in the multispecies-UDRGM by means of 22x2 lookup-tables. This method is a practical, common solution for CFD simulations ([32] [33] [34]). The difference from previous investigations is that in the approach presented here the properties of both phases extend in the metastable regions, down to the corresponding Spinodal lines. The look-up tables are constructed

18

with step sizes in terms of temperature and pressure of 1K and 1bar. In this respect, a sensitivity analysis performed in [18] showed that this step size was the best trade-off between computational time and accuracy. Moreover, the mixture model employed in the present work has shown problems of numerical stiffness in cases where the diffuser is choked (see section 4.1 and 4.2). Consequently, a number of trials were made to devise the convergence strategy with the best trade-off in terms of stability and convergence speed. This strategy resulted in the following steps:

- Set 1st order discretization to all equations

- Set under relaxation factors to 0,5 with the exception of the swirl velocity equation which should be set as low as 0,2 or 0,1

- Initialize the solution by using the Fluent hybrid initialization approach (here, it is important to set a 0 value to the dummy species mass fractions)

- Patch the initial temperature field equal to the motive inlet temperature and the gas volume fraction to values around 0.7

- Set CFL to 0.1 or lower for the first 10 000 iterations, then increase up to max CFL = 0.5 (or 0.2 for cases with low pressure lift, see section 4.1)

- Run until convergence

- switch to 2nd order discretization and run again until convergence

- Increase under-relaxation factors and CFL to check that a stable solution is found

By using this converge procedure, the mixture model computations resulted in around ~2500 Cpu/h for each simulated case, which amounts to nearly 8-10 days of calculations on a 12 cores workstation. This value is ten times higher than the time needed for the convergence of the HEM scheme. However, new simulations that are currently being performed on different ejector geometries are showing that the mixture model can also reach convergence in around 250-300 Cpu/h. The main differences between these new geometries and that presented in this paper is related to the absence of a swirled suction entrance and the presence of a smaller thickness of the nozzle trailing edge. Therefore, it is very likely that the slow convergence rate be caused by instabilities induced by pressure fluctuations at the nozzle exit (e.g., vortex shedding) or by an increased numerical stiffness produced by the inclusion of the swirl velocity transport equation.

19
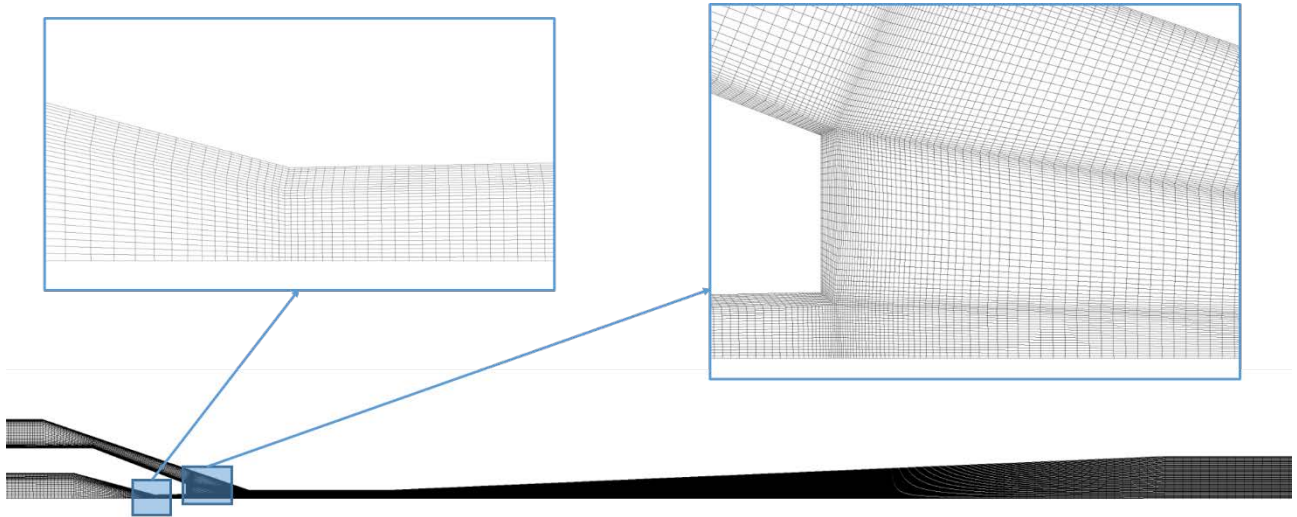
**Figure 8 - Ejector Mesh with detail near the motive nozzle exit**

3.3 Sensitivity Analyses

Several preliminary calculations were performed in order to test the model sensitivity to the following parameters:

- Mesh refinement;

- Evaporation and condensation factor σ_e, σ_c;

- Suction flow swirl.

A mesh sensitivity analysis was carried out for Case 29, using three different meshes with 25000, 50000 and 100000 quadrilateral elements.

Figure 10 (top) shows the pressure profiles along the ejector axis obtained with the different meshes. The three meshes basically return the same results in terms of pressure. Moreover, the variation of the computed mass-flow rates between the 50000 and 100000 element meshes are approximately 0.5% and 1.5% for motive and suction flows, respectively. The same variation is approximately 1.3% and 2.3% between the 25000 and 100000 meshes. Consequently, the intermediate mesh was selected for all the analyses.
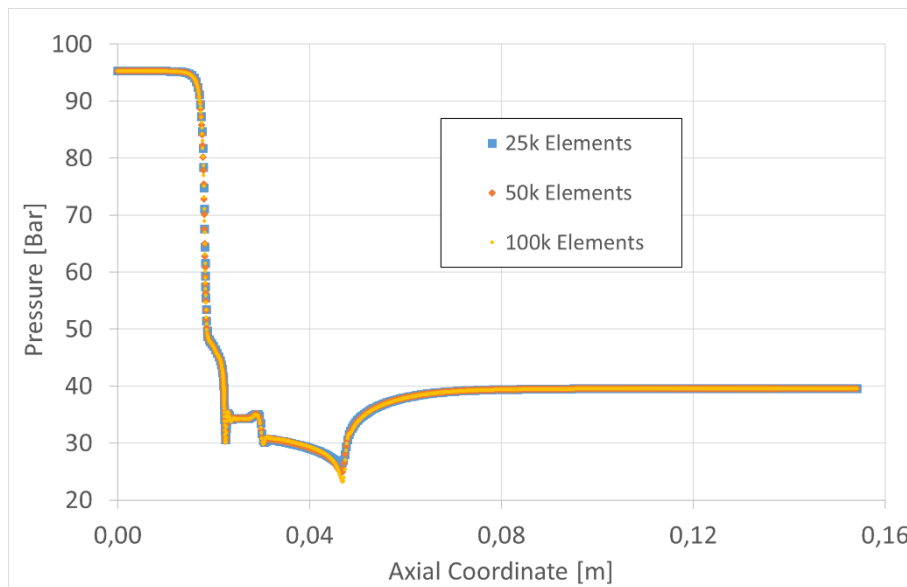
Figure 9 – Pressure profiles along the ejector axis for three different mesh refinements

For the condensation factor, a sensitivity analysis was carried out by varying its order of magnitude from 0.1 to 10000. Figure 10 (top) shows the resulting pressure profiles at the ejector wall for the extreme values of $\sigma_c = 0.1$ and $\sigma_c = 10000$. As can be observed, the profiles are coincident. Moreover, the mass-flow rates turn out to be insensitive to variations of the condensation factor. For instance, the suction stream mass-flow rate resulted in a change of less than 0,05% in passing from $\sigma_c = 0.1$ to for $\sigma_c = 10000$.

Figure 10 (bottom) illustrates the trend of the liquid volume fraction at the ejector wall (a similar trend is found along the axis). As can be observed, the variation of the condensation factor produces different values of volume fraction at the ejector outlet, which change from 0,144% to 0,16% in passing from $\sigma_c = 0.1$ to for $\sigma_c = 10000$ (nearly 11% increase). Unfortunately, no experimental measurement is available for liquid volume fractions and the choice of one value or another for σ_c would be in any case arbitrary. In addition, high values of σ_c were found to induce numerical instabilties and oscillating behavior during convergence, especially in cases where strong shocks are present inside the computational domain (e.g., when the mixing chamber is choked). Consequently, a value $\sigma_c = 0.1$ was selected for all the simulated cases in order to improve the numerical stability of the simulations.

The analyses presented above indicate that the condensation coefficient has a limited impact on the final computational flow field, at least for what concerns the quantities that are measured in the present experimental setup (mass flow rates and pressures). Conversely, the evaporation factor σ_e was found to have a substantial

21

influence in determining the whole ejector behavior, by changing the motive nozzle mass flow rate as well as the void fraction distribution along the ejector. Therefore, the selection of this parameter must be done with great care. Herein, the value of σ_e was tuned to match the measured mass-flow rates of the motive nozzle. A more detailed discussion on the significance of the condensation and evaporation factors tuning is provided in section 4 and 5.
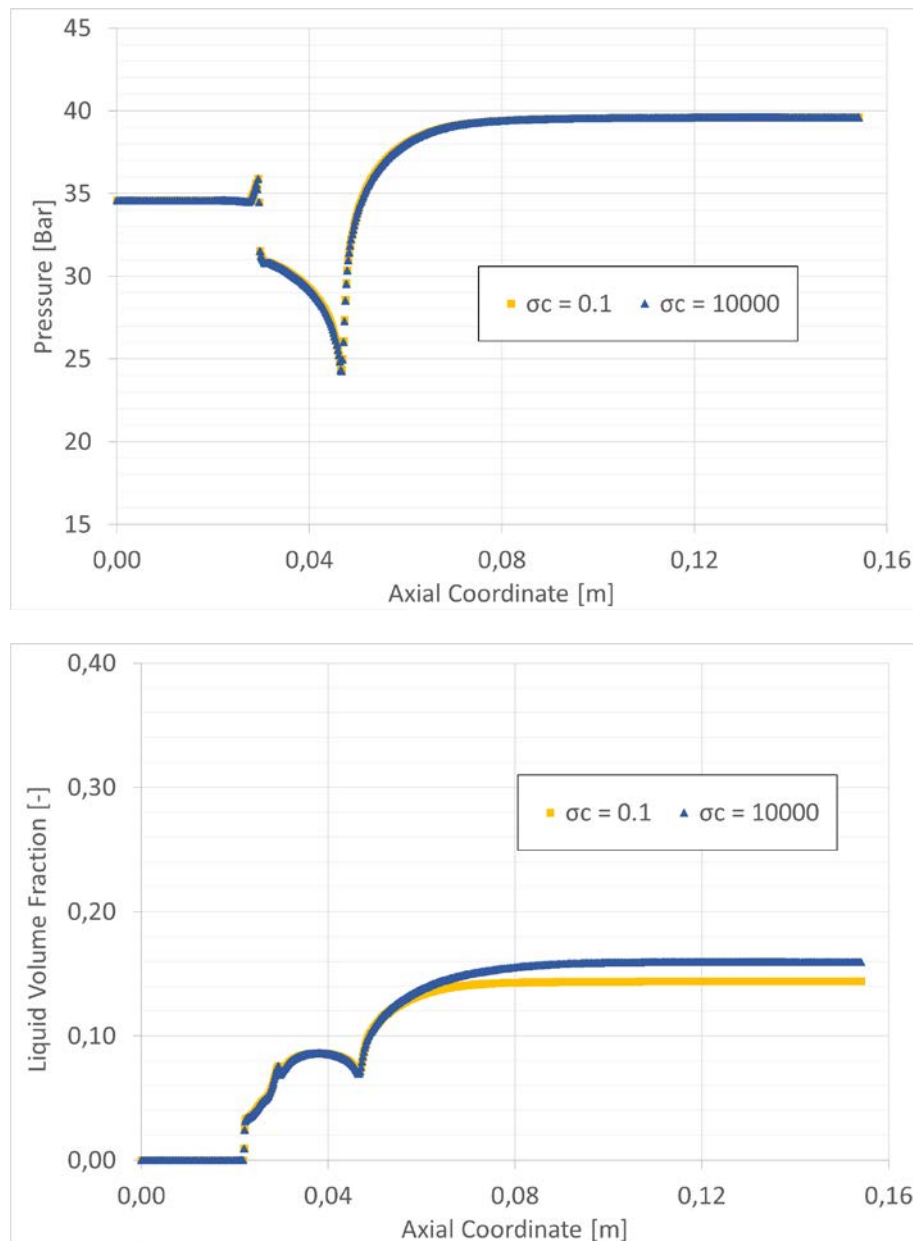
Figure 10 – Condensation factor sensitivity: pressure profiles along the ejector wall (TOP); Liquid volume fraction at the ejector wall (BOTTOM)

22

Finally, the swirl of the suction stream was modeled by making use of the axisymmetric swirl approximation. This approach consists of solving an additional transport equation for the conservation of the tangential momentum [17]. It is worth remembering that, in order to achieve a better representation of the flow, a full 3D analysis would be necessary. Herein, the choice of the 2D axisymmetric swirled domain was mainly dictated by the need for maintaining a reasonable computational cost.

The swirl at the suction inlet was imposed by setting the value of the velocity component in the axial, radial and tangential directions. In particular, the components were varied in order to maintain the geometrical angle of 62.5° between the radial and tangential axes. Moreover, the angle between the radial and axial direction was analyzed by a sensitivity analysis. Figure 11 (top) shows the wall pressure profiles for different angles (the case with angle 0° represents the solution without any swirl). Clearly, the pressure is not significantly affected by this variation. By contrast, the suction flow rate is slightly influenced by a change in the radial angle, as shown in Figure 11 (bottom). As can be seen, the secondary stream mass-flow rate increases with higher angles and the difference with the experiments diminishes. Consequently, the 70° angle was selected for all calculations (including those with the HEM).

23
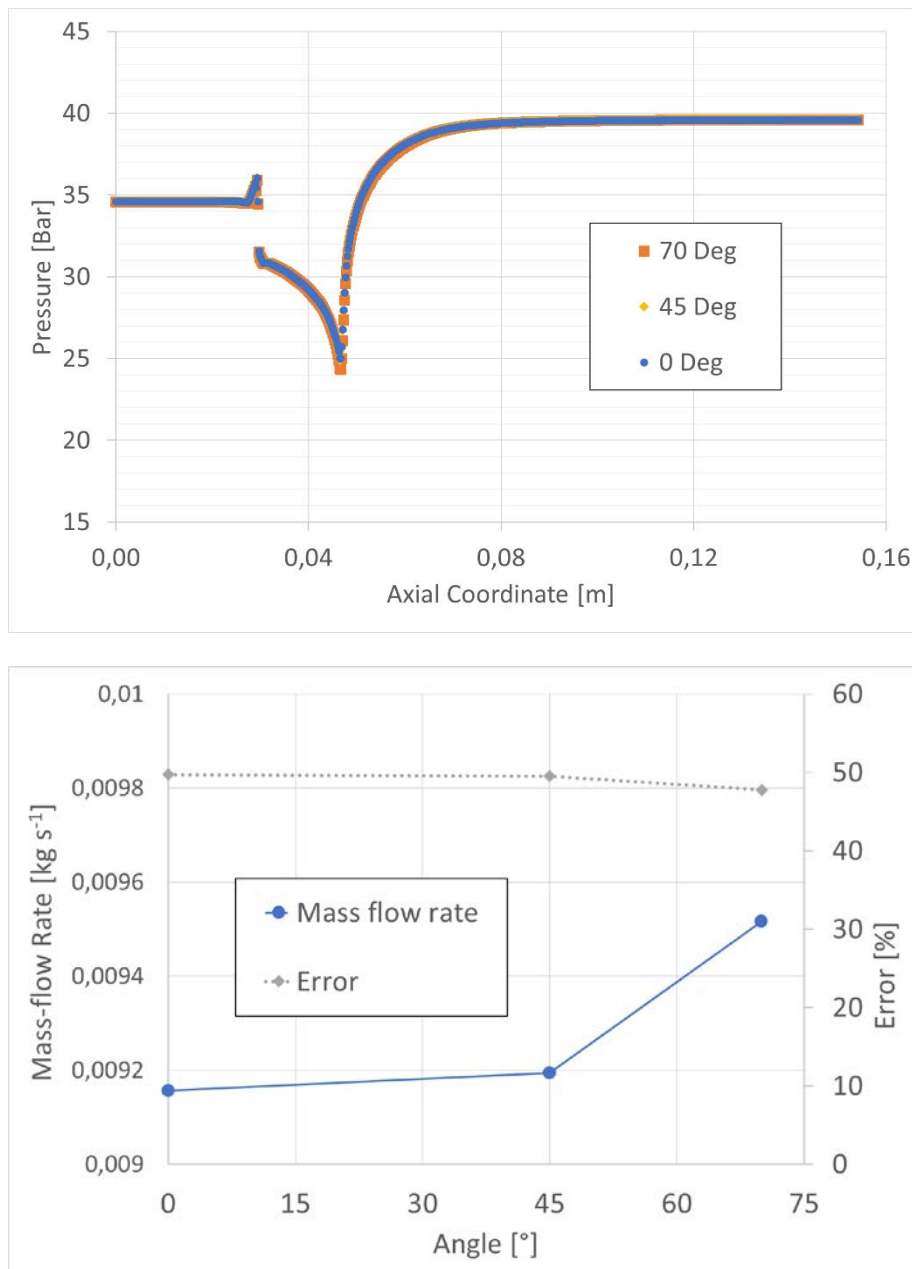
Figure 11 - Pressure profiles at ejector wall for different angles for Case 29 (TOP); Computed suction mass-flow rates at different angles between the radial and axial directions (BOTTOM)

4. RESULTS

4.1 Mass flow rates

One of the main criteria to evaluate the performance of the numerical model presented here is accuracy in the predicted mass flow rates. Figure 12 shows the trend of ER vs pressure lift for both the mixture and HEM models. Noticeably, the mixture model improves over the HEM in terms of ER predictions, with an average difference of around 19% and 48% for the former and latter, respectively. Moreover, the mixture model appears

24

to more closely reproduce the decreasing flow rate trend with the pressure lift, at least for the supercritical curve.

Nevertheless, these results must be analysed by keeping in mind that the evaporation factor of the mixture model was specifically tuned to achieve accuracy in the primary flow rates of less than 2%.

In order to analyse the effect of this tuning, the comparison between the two models is presented in terms of motive and suction flow rates, as illustrated in Figure 13. In addition, Table 5 provides the differences between the experimental and numerical results for all the simulated cases (the table gives also the values of σ_e employed in the mixture model for each simulated condition).

As can be seen, the motive flow rate is a major source of error for the HEM, whereas the mixture model basically matches the experiments. Although this result is achieved thanks to the specific tuning, the value of the evaporation coefficient had to be changed only in passing from supercritical to subcritical conditions. In particular, σ_e is higher in supercritical cases. This behaviour is physical as the increase of the evaporation factor leads to a reduction of the metastability effect and faster evaporation (σ_e is basically the inverse of a relaxation time to equilibrium). This means that the model correctly reproduces the tendency of a near-critical flow to become closer to an equilibrium phase change. Similar conclusions were found by Palacz et al. [35] by comparing the results obtained with a HEM and an HRM.

In terms of secondary mass flow rates, the mixture model improves on the HEM by reducing the differences by more than a half. In this case, no tuning is involved for the mixture model parameters and it is reasonable to attribute the positive result to the enhanced capabilities of the model to reproduce the flow features inside the mixing chamber. Nevertheless, the differences with experiments are still between 10-17%. Much of this discrepancy may come from having adopted a 2D swirled axisymmetric domain (as opposed to a full 3D simulation). Moreover, the entrainment of the secondary flow depends very much on the complex two-phase and compressible interactions that occur inside the turbulent mixing layer. Among others, these comprise interactions between bubbles, turbulence and shocks that are barely captured by simplified averaged CFD approaches. However, since the developed model was constructed via UDFs, some attempts could be made in future studies to include turbulence corrections that account for these effects.
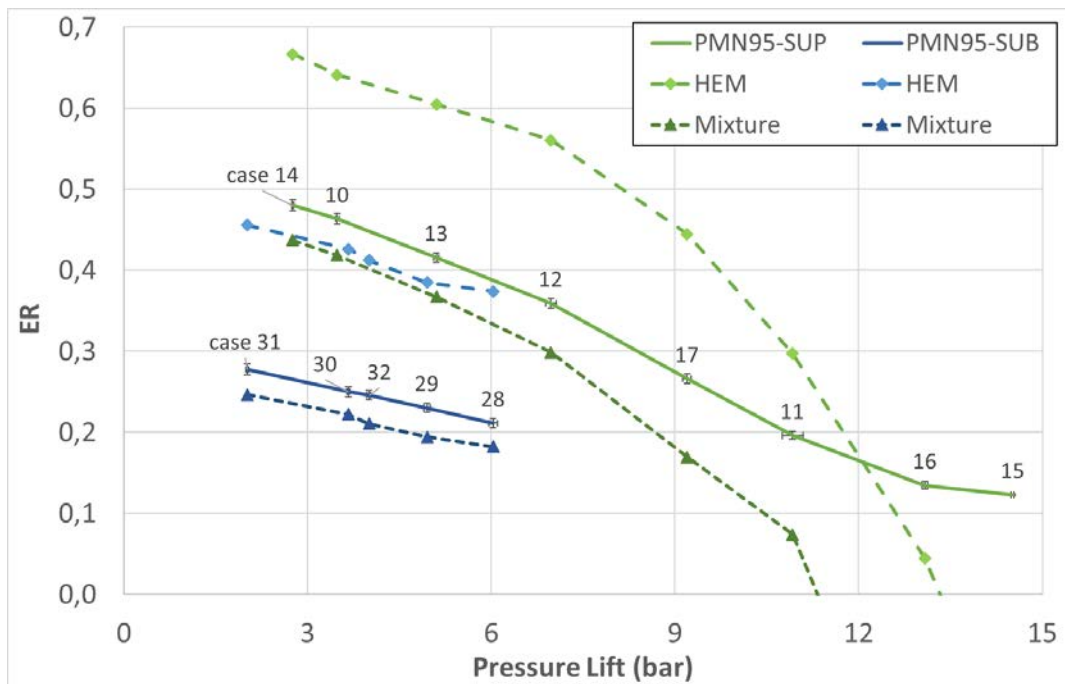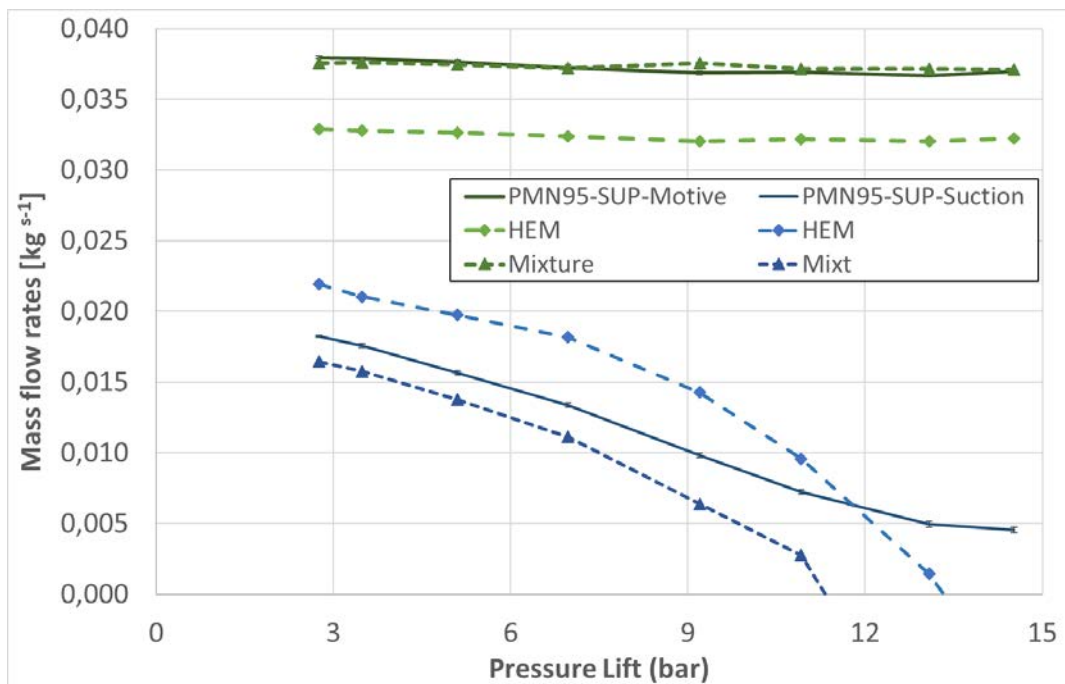
25

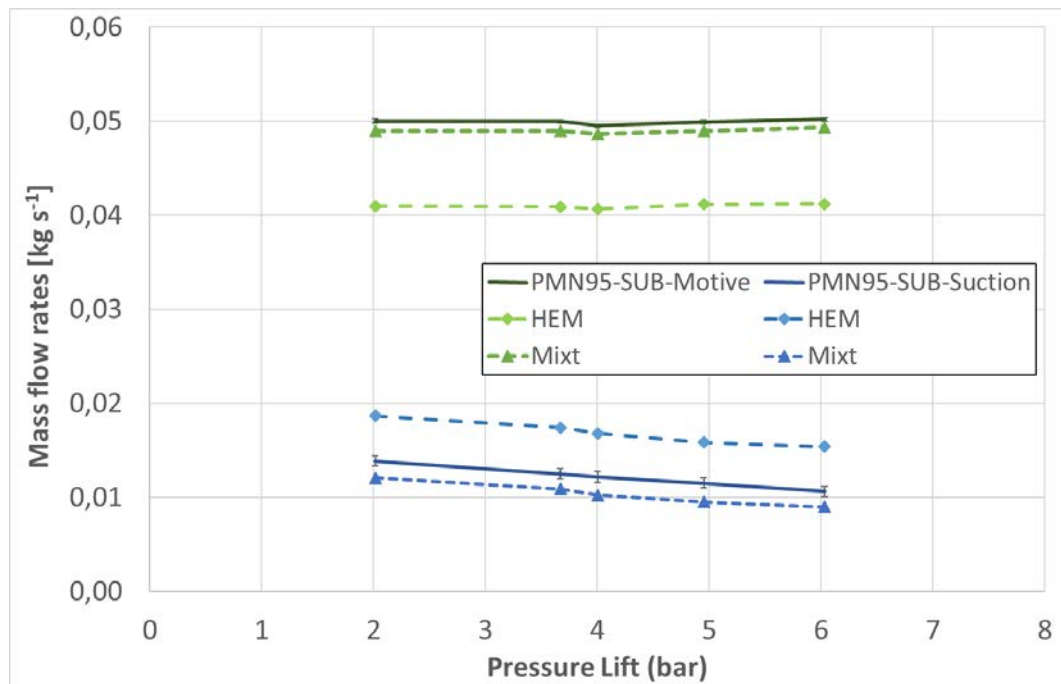**Figure 12 - ER vs pressure lift: comparison of CFD and experimental trends**

26

Figure 13 - mass flow rates vs pressure lift: comparison of CFD and experimental trends for the supercritical (top) and subcritical cases (bottom)

	Exp	HEM					Mixture				
Case	MN conditions	MN err [%]	SN err [%]	Flow rates Conditions	Mass imbalance	σ_e	MN err [%]	SN err [%]	Flow rates Conditions	Mass imbalance
14	Supercritical	-13,3	20,4	Steady, Choked diffuser	-1,8E-07	600000	-1,0	-9,8	Steady, Choked diffuser	2,8E-05
10	Supercritical	-13,4	19,8	Oscillating outlet, Choked Diffuser	4,3E-04	600000	-0,7	-10,2	Oscillating outlet, Choked diffuser	2,4E-05
13	Supercritical	-13,2	26,3	Steady	-6,5E-08	600000	-0,4	-12,1	Steady	-3,0E-08
12	Supercritical	-13,0	35,8	Steady	2,5E-07	600000	-0,1	-16,9	Steady	5,4E-05
17	Supercritical	-13,1	45,3	Steady	-1,3E-06	600000	1,8	-35,0	Steady	2,4E-05
11	Supercritical	-12,9	32,2	Steady	-9,1E-07	600000	0,6	-62,0	Steady	2,6E-06
16	Supercritical	-12,7	-70,8	Oscillating suction	1,3E-03	600000	1,3	-	Unsteady, Suction Backflow	-2,8E-03
15	Supercritical	-12,8	-	Suction Backflow	1,3E-04	600000	0,3	-	Unsteady, Suction Backflow	2,7E-04
31	subcritical	-18,1	34,4	Steady, Choked Diffuser	-3,5E-04	100000	-2,1	-13,0	Steady, Choked Diffuser	-2,6E-03
30	subcritical	-18,1	39,4	Steady	1,3E-07	100000	-2,0	-13,0	Steady, Choked diffuser	-2,8E-04

27

32	subcritical	-17,8	37,9	Steady	-2,7E-08	100000	-1,8	-15,8	Steady	3,0E-05
29	subcritical	-18,2	42,1	Steady	1,0E-07	100000	-2,0	-17,3	Steady	-3,7E-04
28	subcritical	-18,0	45,0	Steady	-8,9E-06	100000	-1,7	-15,2	Steady	-4,4E-04

Table 5 – Difference in mass-flow rates predictions between HEM and Mixture model
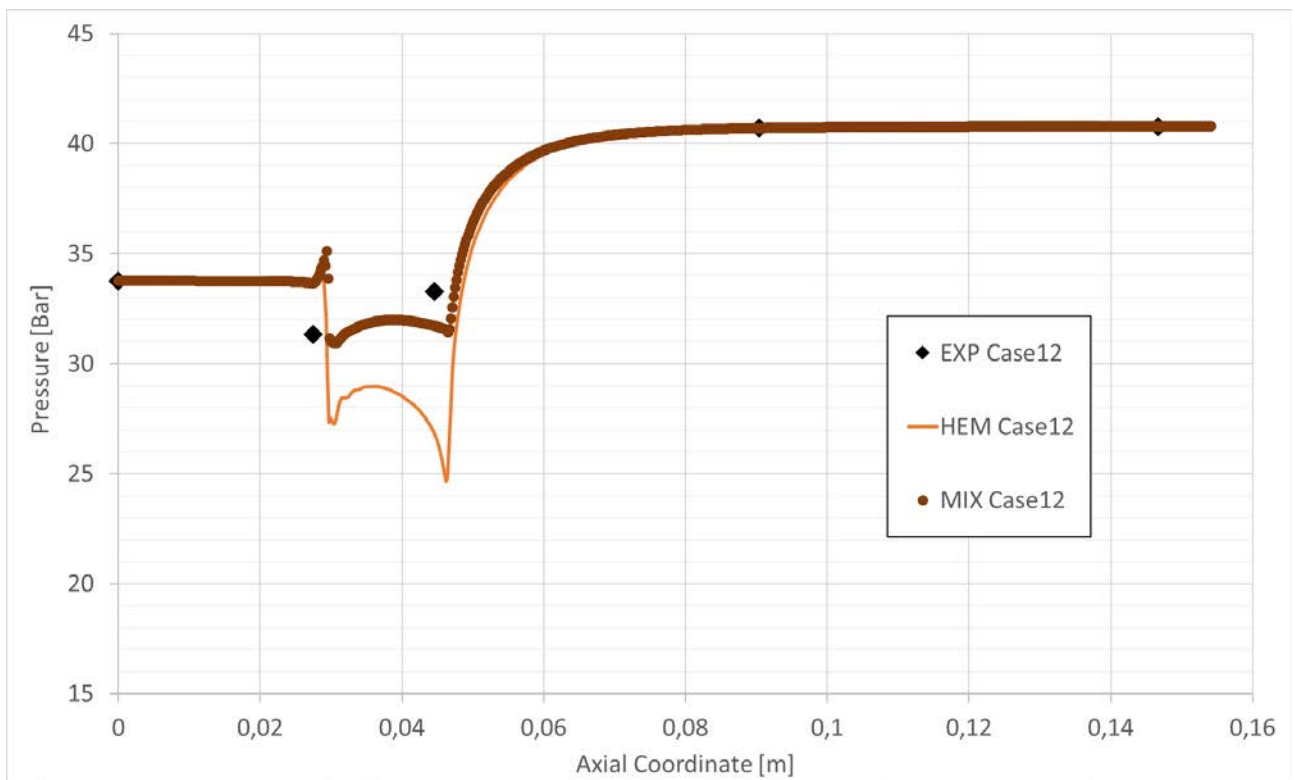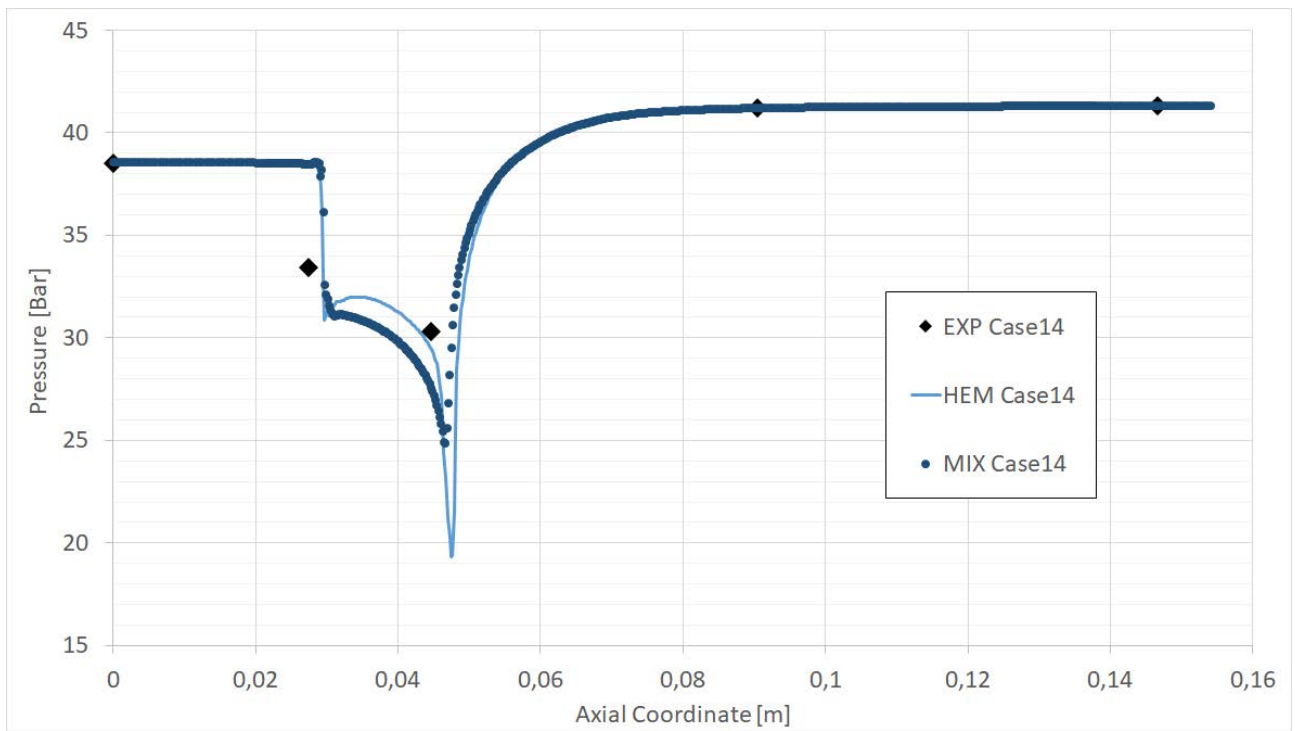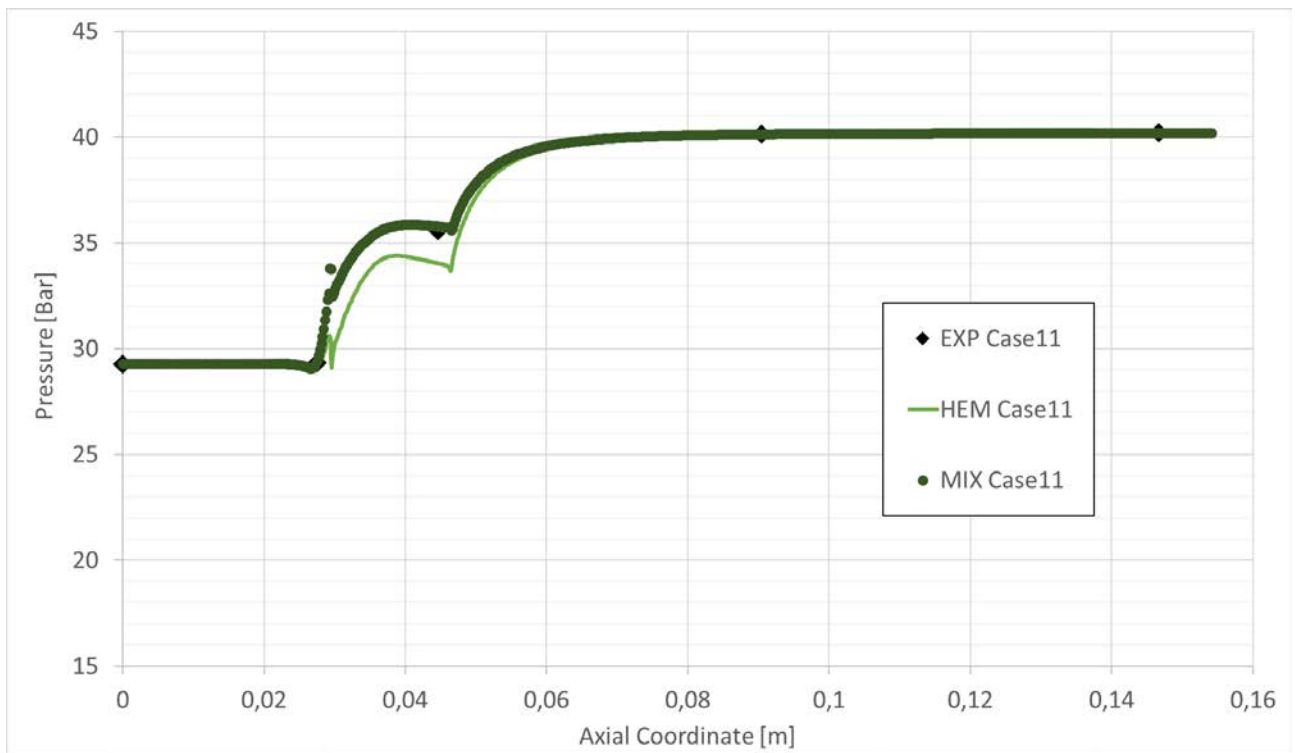
4.2 Pressure Profiles

Figure 14 and Figure 15 show the comparison between the numerical and experimental wall pressure profiles for some representative supercritical and subcritical cases, respectively. The zero of the axial direction is located at the beginning of the computational domain of Figure 8 and corresponds to the position of the first pressure transducer. The second and third sensors are located at the beginning and end of the constant section mixing chamber, whereas the fourth and last are placed in the middle and end of the diffuser.

In general, both models seem to qualitatively reproduce the trend of the static pressure along the ejector. The mixture model appears to slightly improve over the HEM predictions, except perhaps in case 14 that has the highest suction pressure among all the supercritical cases. In this case, the diffuser is choked (see Table 5) and the suction flow expands and accelerates faster than in other conditions. In turn, this should lead to a reduced effect of non-equilibrium effects during the expansion inside the mixing chamber. As a result, the pressure profiles predicted by both the HEM and Mixture Model seem to approximately follow the same trend.

This agreement between the two models reduces as the pressure lift decreases and in case 12 the difference between the two approaches becomes evident, with HEM that overestimates the depressurization with respect to both experimental and mixture model trends. In all cases, the pressure variations of the HEM are steeper with respect to the mixture model scheme. This difference is most likely caused by the absence of the relaxation time typical of non-equilibrium phase change models (see next section).

In subcritical conditions, the difference between CFD and the experiments is reduced and deciding which model performs better becomes less obvious. In addition, this ambiguity is worsened by the fact that the number of pressure transducers does not seem to be really adequate for an accurate estimation of the quality of the numerical results. More pressure sensors and possibly thermocouples should be used in future experimental test-cases to obtain a better resolution of the profiles at the ejector wall. However, this may be difficult because of the small dimensions of the ejectors tested.

28

29

Figure 14 - Ejector wall pressure profiles for supercritical inlet conditions

30
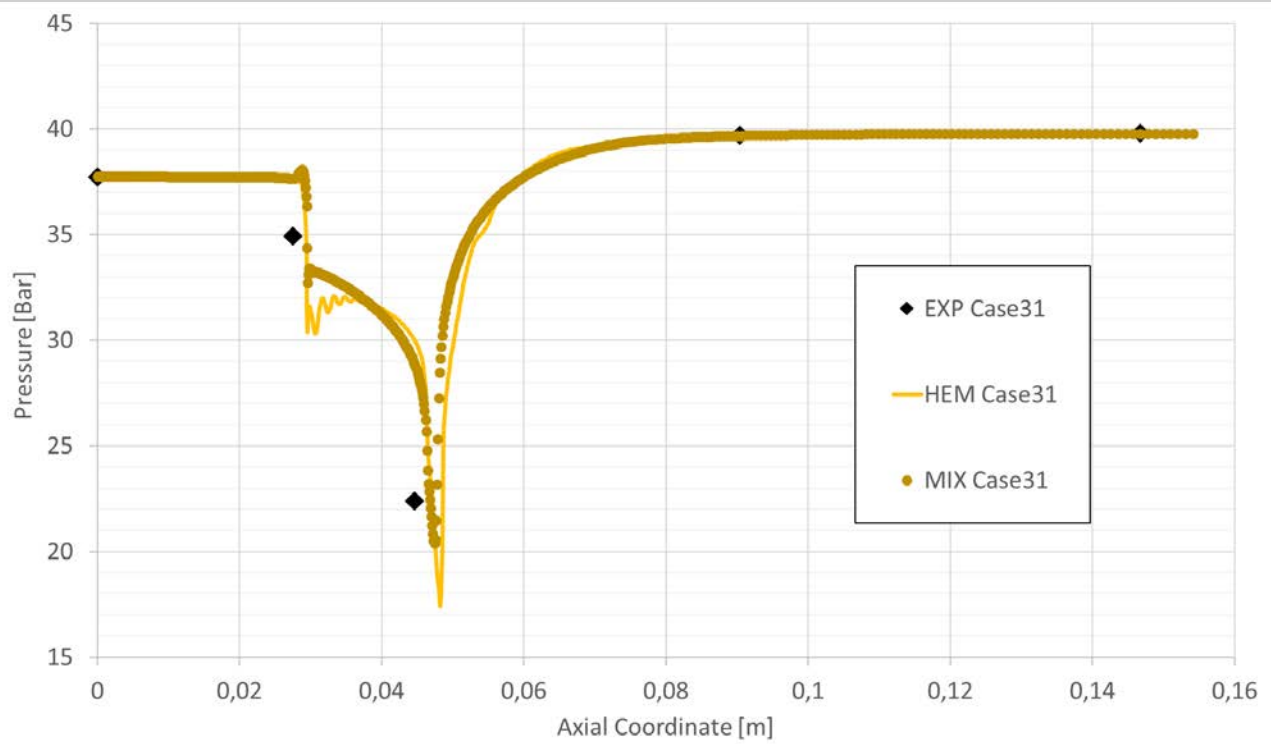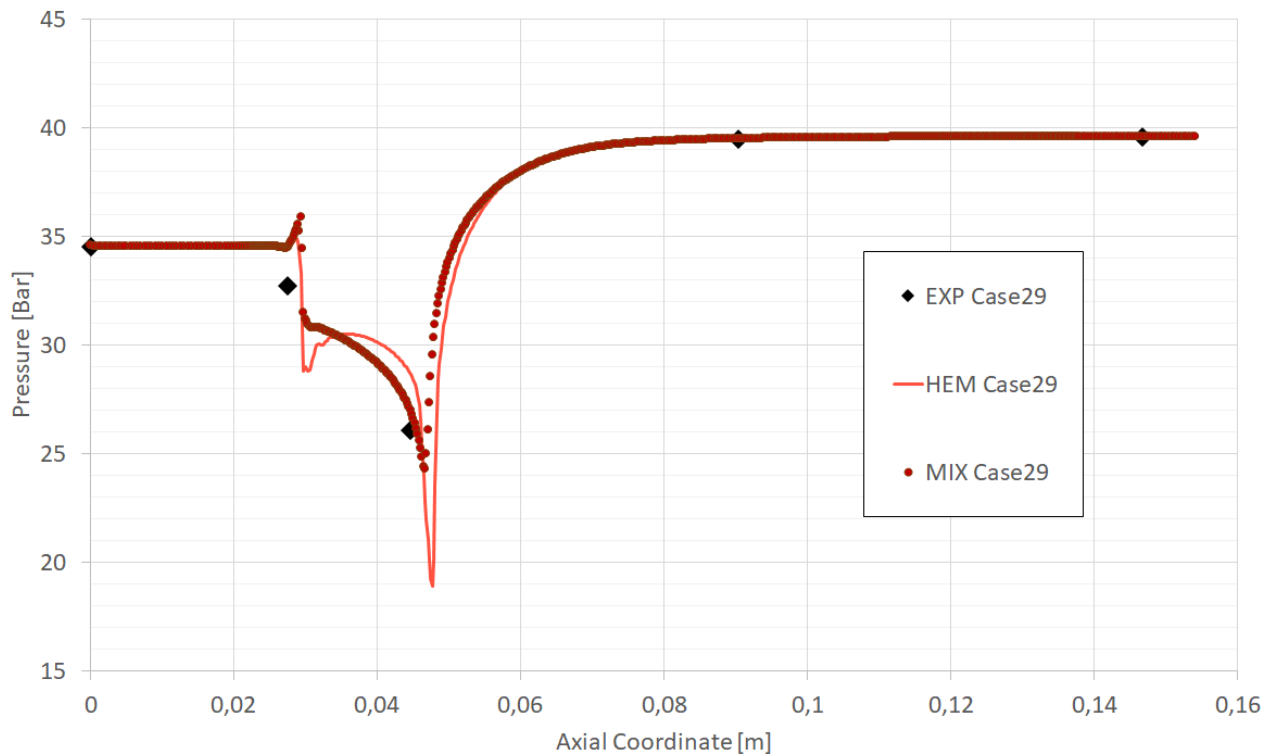
Figure 15 - Ejector wall pressure profiles for subcritical inlet conditions

4.3 Ejector internal flow field

Figure 16 shows the density contours for Case 29 with HEM on the top half and the Mixture model on the bottom half. The strength of shocks and expansion waves at the nozzle exit is higher for the HEM (likewise, the shock train at the beginning of the diffuser section is more evident in the case of the HEM). Similar behaviour was found in previous comparisons between equilibrium and non-equilibrium models [33] [36] and may result from a faster heat release in the case of equilibrium phase change. The relaxation introduced into the mixture-model approach acts as a damping of the mass-transfer related gradients.

It is also interesting to analyse the differences between the supercritical and subcritical cases. This is done in Figure 17, in which the density contours are compared for Cases 14 and 29. From the figure it is evident that the strength of both the shock and expansion waves is higher in supercritical case (Case 14).
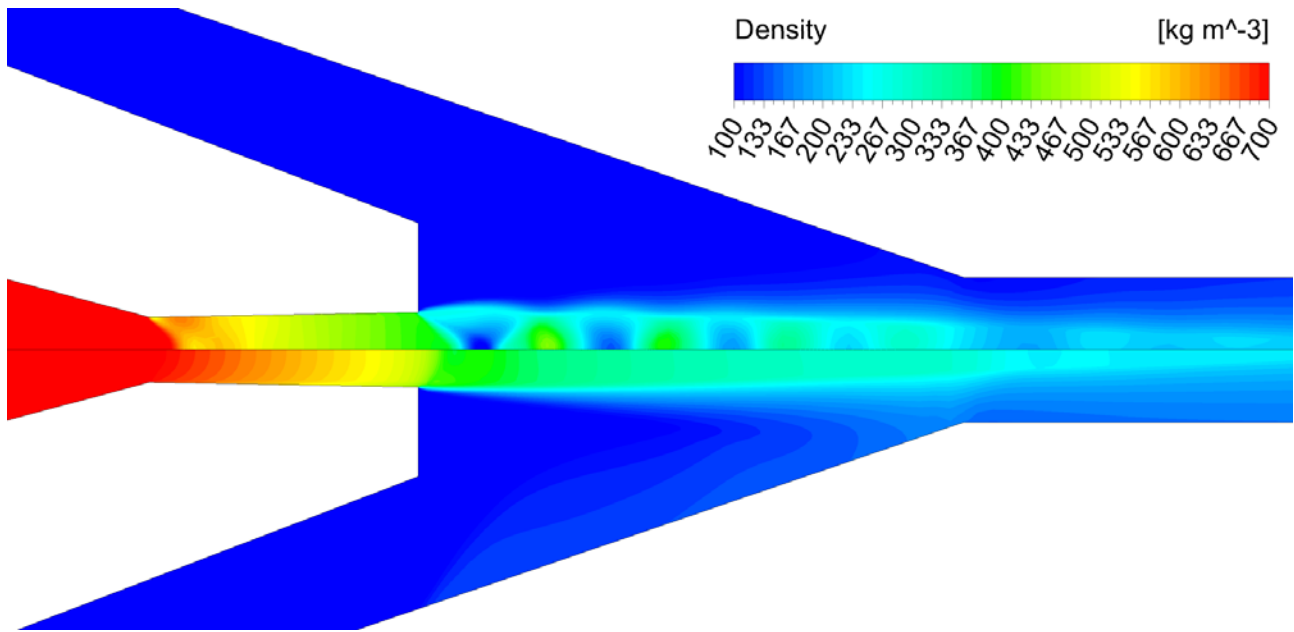
31

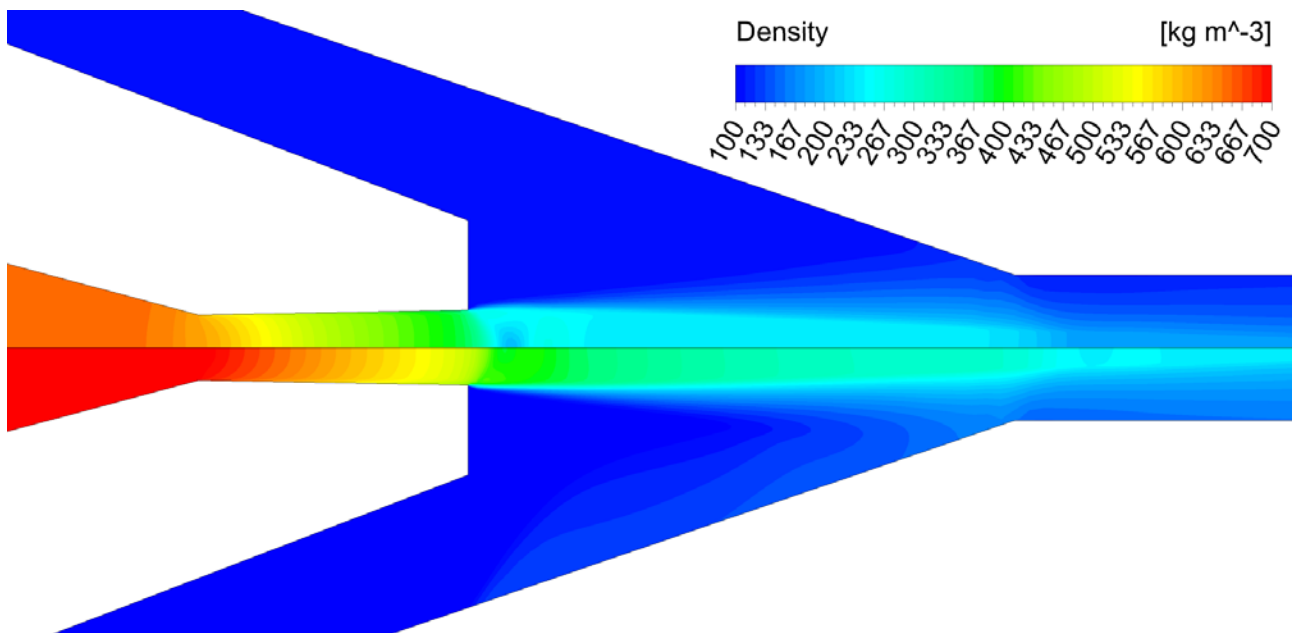**Figure 16 - Density contours for Case 29 – subcritical. HEM (TOP), Mixture-model (BOTTOM)**

Figure 17 - Density contours of Mixture model. Case 14 - supercritical (TOP), Case 29 - subcritical (BOTTOM)

Figure 18 compares Cases 14 and 29 in terms of vapour volume fraction. When looking at the figure, a delayed phase change is visible in the case of subcritical operations. This delay results in an increased motive mass-flow rate with respect to supercritical conditions, which may be due to a shift of the choking section further downstream. In Figure 19 the same vapour volume fraction trends are shown along the nozzle axis in order to

32

better highlight the differences between the two cases. Clearly, the supercritical case presents a shock right after the nozzle exit. Moreover, an increased evaporation is seen at the nozzle exit for supercritical conditions. Finally, Figure 20 presents a comparison of the Mach contours obtained with two different sound speed formulations. The bottom half shows the Mach resulting from the Wallis formulation, equation 5, whereas in the top half the Mach is calculated following the speed of sound definition provided by Brennen [37]:

$$\frac{1}{\rho a^2} = \frac{\alpha_v}{P}\left[(1 - \varepsilon_v)f_v + \varepsilon_v g_v\right] + \frac{1 - \alpha_v}{P}\varepsilon_l g_l \qquad (6)$$

where f and g are functions of the thermodynamic properties of the fluid while ε_v and ε_l represent the portion of interface, i.e., the part of each phase that interacts with the other phase. The equation was eventually simplified according to the suggestions of the author:

- $f_v \approx 1, g_v \approx 1$;
- $\varepsilon_v \approx (1 - \alpha_v), \varepsilon_l \approx \alpha_v$;
- $g_l \approx 2.1(P/P_{critical})^{-0.566}$

In addition, Figure 20 shows the sonic line calculated with the two formulations and superimposed to the Mach number field.

As can be seen, the use of the Brennen equations results in higher Mach numbers with respect to the Wallis formulation. In particular, the use of the Wallis equation produces a subsonic region all over the motive nozzle divergent section as well as in the mixing chamber. Clearly, this represents an approximation because both the primary nozzle and diffuser are choked in this condition (this can be demonstrated by checking the mass flow rate insensitivity to downstream pressure change). As previously reported by Giacomelli et al. [23], the Brennen formulation appears to be more coherent with physical behaviour as it better reproduces the transition from subsonic to supersonic regions.

Finally, the use of a more physically accurate formulation for the speed of sound for the mixture could also benefit the stability and convergence rate of the simulations. As a matter of fact, flashing evaporation tends to be a very stiff process from the numerical point of view, due to the fast change in local densities and

33

temperatures. Unlike a normal compressible jet, the presence of shocks can lead to downstream condensation further destabilising the numerics.

Not surprisingly, the numerical simulations with the mixture model have shown some numerical instabilities as well as slow convergence rates, especially in cases with low pressure lift where the simulated ejector conditions produce a choked flow inside the mixing chamber. This problem was absent when the same model was used to analyse the flashing nozzle described in [23], which suggests that these instabilities are likely due to the large density variations that occur across shock diamonds and shock trains that appear in the ejector mixing chamber and diffuser, respectively.

Unfortunately, in ANSYS Fluent the formulation for the mixture speed of sound is not modifiable by the user. Therefore, it was not possible to improve the numerical stability of the simulation by using a more accurate equation. However, it should be noted that the choice of the sound speed formulation does not influence the final converged flow field, as this is only determined by the governing equations together with the equation of state. Nevertheless, the use of a more accurate definition, such as the one from Brennen, is recommended for a more meaningful post processing of the numerical results.
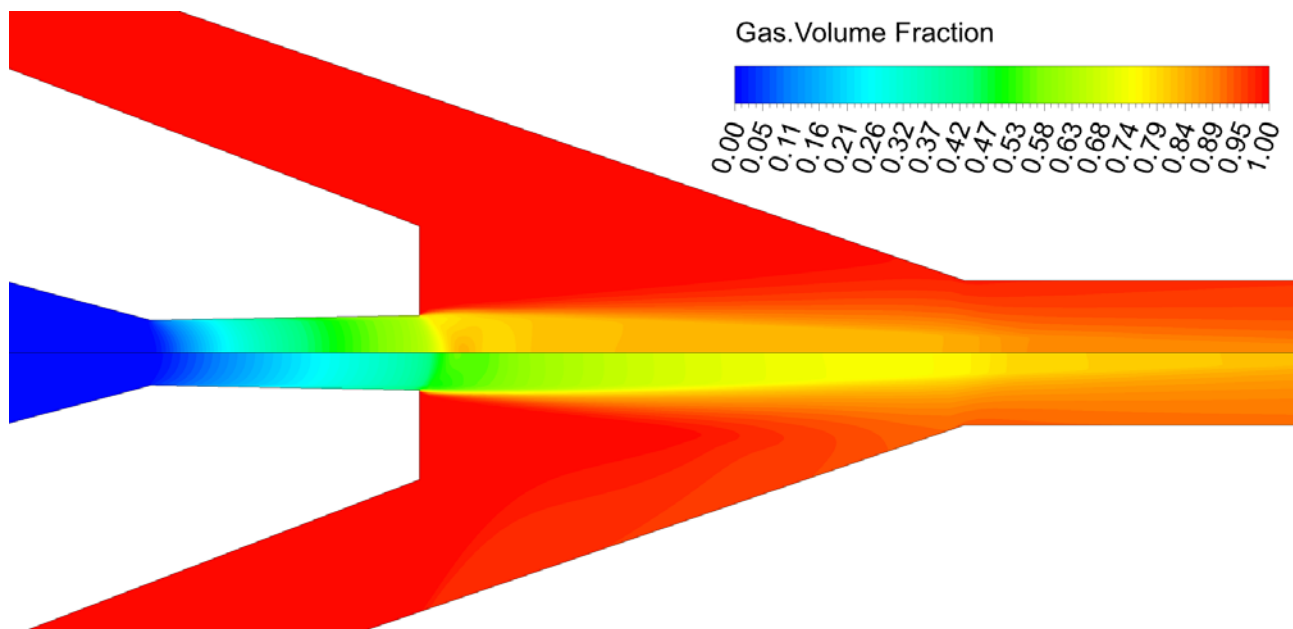
Figure 18 - Vapor volume fraction contour for the Mixture model (nozzle and mixing chamber). Case 14 - supercritical (TOP), Case 29 - subcritical (BOTTOM);

34
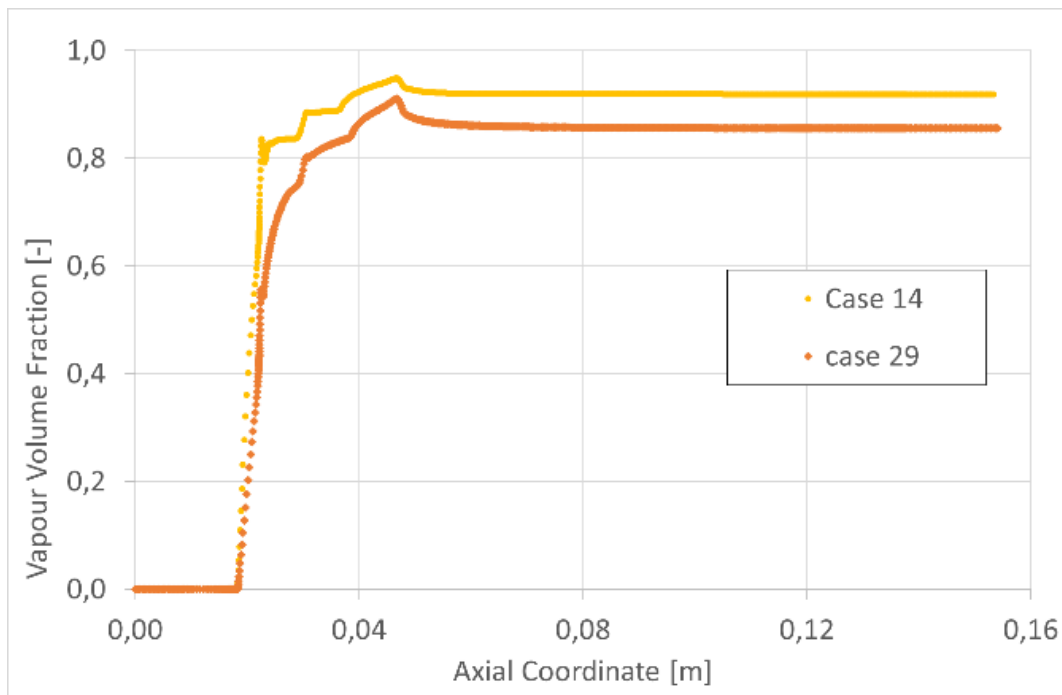
Figure 19 - Axial trends of vapor volume fraction for the Mixture model (whole ejector lenght). Case 14 - supercritical (TOP), Case 29 - subcritical (BOTTOM)
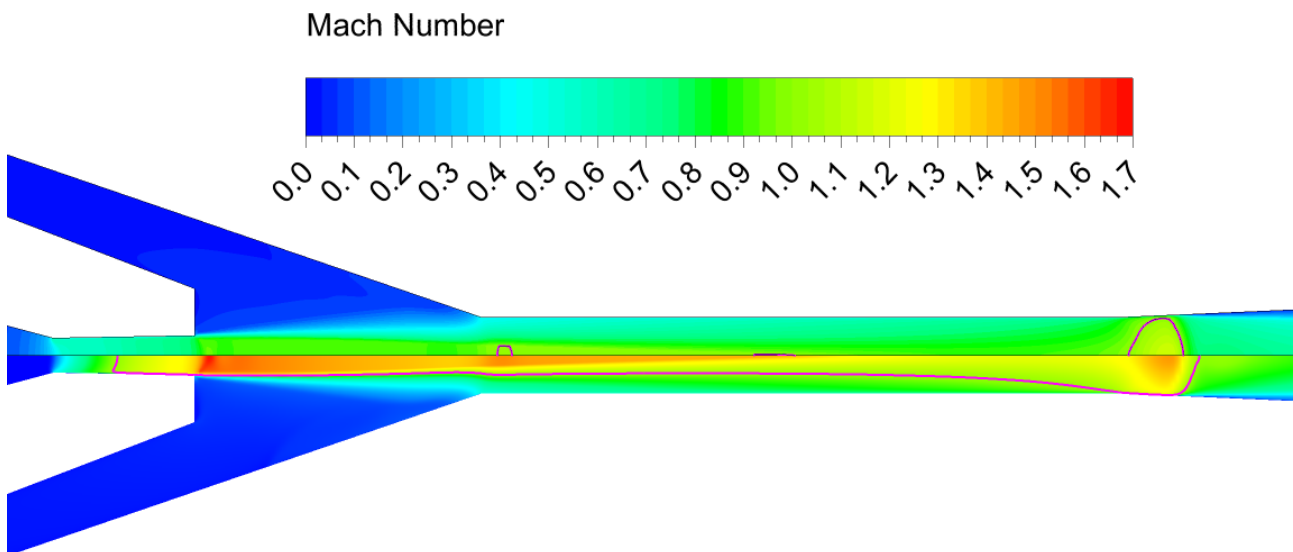
Figure 20 - Mach number and sonic lines (in violet) for different speed of sound formulations for Case 14. Brennen equation (TOP), Wallis equation (BOTTOM)

35

5. HEM vs MIXTURE MODEL: DISCUSSION

From a purely numerical point of view, the comparison between the two models has shown that the HEM is very fast and stable, whereas the mixture model numerics is more stiff and susceptible of divergence.

The lower stability of the mixture model is more evident when the ejector operates in double-choking condition and may be due to the large density and temperature variations that occur across the shocks in the ejector mixing chamber and diffuser. The additional coupling with the swirl velocity transport equation and a non-optimal definition of the mixture speed of sound may also contribute to slow down the convergence rate of the simulations.

The use of constant evaporation and condensation coefficients may aggravate these instabilities by preventing the local modulation of the phase change relaxations times. For instance, in the present study the evaporation coefficient is tuned on the nozzle throat flashing expansion and its value may be overestimated for regions where the pressure decrease is less rapid. One way to modulate the phase change parameters would be to keep track of the amount of interacting surfaces. This improvement may be crucial in view of the fact that the two-phase topology dramatically change from dense regions inside the primary nozzle to dispersed mixture zones inside the mixing chamber and diffuser. However, models that can transport the interface density are still under development in low speed applications and the extension to high Mach number flows may represent an extremely complex task, which will nevertheless be attempted in future works.

In terms of accuracy, the mixture-model has shown improvements with respect to the HEM, especially for mass-flow rates predictions. In particular, the performances of the HEM are rather poor in subcritical regions where the assumption of instantaneous phase change is less reliable. Despite this, the comparison on the accuracy is partially impaired by the tuning that can be performed on the phase change parameters of the mixture model. As a matter of fact, the experimental validation presented in this study must be seen as partly providing different information on the two models: whereas for the HEM we are testing its predicting capabilities, with the mixture model we can more realistically answer the question on how good the scheme is in fitting the experimental data.

Yet, this view too may be less clear-cut. Indeed, the predictive capabilities of the mixture model arise in consideration of the fact that the values for the evaporation coefficients were quite stable in this study (i.e., they had not to be recalibrated for each case, but only in passing from super to subcritical conditions).

36

Moreover, the suction flow rates were generally well reproduced without the need for a specific calibration. Finally, the possibility of adjusting the phase change parameters may itself be considered as an advantage of the mixture model, because it allows extending the range of operating regimes that can be simulated beyond that of the simpler HEM (which is basically limited to the region the critical point).

In any case, a more accurate assessment of the models' accuracy may require better resolution of the wall profiles, as well as information on wall temperatures and outlet void fractions. This last in particular would be extremely useful in order to understand the order of magnitude of the evaporation coefficient, which was considered negligible in the present investigation.

6. CONCLUSION

The flash evaporation process in the R744 ejector was investigated both experimentally and numerically. Experimental data for mass flow rates and wall pressure profiles were compared against CFD simulations employing an HEM and a newly developed mixture model. The first assumes equilibrium phase change while the latter includes non-equilibrium features and can describe the fluid properties both in supercritical and metastable conditions.

In terms of numerical performances, the HEM has proved to be faster and less prone to divergence than the mixture model. In terms of accuracy, the Mixture-model has shown improvements over the HEM, especially in predicting mass-flow rates and entrainment ratios. The pressure profiles are generally well reproduced by both models, with the mixture model that achieve slightly better agreements than the HEM. However, a more accurate assessment of the numerical models accuracy may require a greater number of sensors, which is difficult to achieve due to difficulties connected to the high pressures and space limitations.

One of the major disadvantage of the mixture model employed in this study is that the evaporation and condensation coefficients require specific calibration, whereas the HEM does not need any particular tuning. On the other hand, the mixture model is flexible in terms of multiphase model selection, and more advanced schemes can be implemented. In particular, introducing the transport of the interface density may represent a promising improvement, as it permits a local modulation of the phase change relaxations times along the different ejector parts, such as in dense regions inside the primary nozzle or downstream of it.

Finally, a comparison between two different equations for the mixture speed of sound illustrates that the Brennen formulation produces substantially better results than the expression derived by Wallis and used by the commercial software.

AKNOWLEDGMENTS

REFERENCES

[1] S. Elbel, «Historical and present developments of ejector refrigeration systems with emphasis on transcritical carbon dioxide air-conditioning applications,» *International Journal of Refrigeration,* vol. 34, n. 7, pp. 1545-1561, 2011.

[2] S. Elbel e N. Lawrence, «Review of recent developments in advanced,» *International Journal of Refrigeration,* vol. 62, pp. 1-18, 2016.

[3] P. Gullo, A. Hafner e K. Banasiak, «Transcritical R744 refrigeration systems for supermarket applications: Current status and future perspectives,» *International Journal of Refrigeration,* vol. 93, p. 269–310, 2018.

[4] P. Gullo, A. Hafner, k. Banasiak, S. Minetto e E. Kriezi, «Multi-Ejector Concept: A Comprehensive Review on its Latest Technological Developments,» *Energies,* Vol. %1 di %212, 406, pp. 1-29, 2019.

[5] G. Grazzini, A. Milazzo e F. Mazzelli, Ejectors for Efficient Refrigeration, Springer, 2018.

[6] M. Nakagawa, M. Berana e A. Kishine, « Supersonic two-phase flow of CO2 through converging-diverging nozzles for the ejector refrigeration cycle,» *International Journal of Refrigeration,* vol. 32, pp. 1195-1202, 2009.

[7] M. Berana, M. Nakagawa e A. Harada, «Shock waves in supersonic two-phase flow of CO2 in converging–diverging nozzles,» *HVAC&R Research,* vol. 15, pp. 1081-1098, 2009.

[8] K. Banasiak, A. Hafner e T. Andresen, «Experimental and numerical investigation of the influence of the two-phase ejector geometry on the performance of the R744 heat pump,» *International Journal of Refrigeration,* vol. 35, pp. 1617-1625, 2012.

[9] Y. Zhu, Z. Wang, Y. Yang e P.-X. Jiang, «Flow visualization of supersonic two-phase transcritical flow of CO2 in an ejector of a refrigeration system,» *international journal of refrigeration,* vol. 74, p. 354–361, 2017.

[10] Y. Liao e D. Lucas, «Computational modelling of flash boiling flows: A literature survey,» *International Journal of Heat and Mass Transfer,* vol. 111, p. 246–265, 2017.

[11] G. Polanco, A. Holdøb e G. Munday, «General review of flashing jet studies,» *Journal of Hazardous Materials,* vol. 173, p. 2–18, 2010.

[12] Q. Le, R. Mereu, G. besagni, V. Dossena e F. Inzoli, «Computational Fluid Dynamics Modeling of Flashing Flow in Convergent-Divergent Nozzle,» *Journal of Fluids Engineering,* vol. 140, pp. 101102-1/22, 2018.

[13] C. Lucas, H. Rusche, A. Schroeder e J. Koehler, «Numerical investigation of a two-phase CO2 ejector,» *International Journal of Refrigeration,* vol. 43, pp. 154-166, 2014.

[14] M. Ghiaasiaan, Two-Phase Flow, Boiling and Condensation in Conventional and Miniature Systems, Cambridge, UK: Cambridge University Press, 2008.

[15] H. Jasak, A. Jemcov e Z. Tukovic, «OpenFOAM: A C++ Library for Complex Physics Simulations,» in *International Workshop on Coupled Methods in Numerical Dynamics*, IUC, Dubrovnik, Croatia, September 19th-21st , 2007.

[16] J. Smolka, Z. Bulinski, A. Fic, A. J. Nowak, K. Banasiak e A. Hafner, «A computational model of a transcritical R744 ejector based on a homogeneous real fluid approach,» *Applied Mathematical Modelling,* vol. 37, pp. 1208-1224, 2013.

[17] ANSYS Inc., ANSYS Fluent Theory Guide, Canonsburg, PA: release 19.0, 2018.

[18] F. Giacomelli, K. Krzysztof Banasiak, A. Hafner, F. Mazzelli e A. Milazzo, «Experimental and Numerical Investigation on an Ejector for CO2 Vapor,» in *Gustav Lorentzen Conference*, Valencia, 2018.

[19] E. W. Lemmon, M. L. Huber e M. O. McLinden, *NIST Reference Fluid Thermodynamic and Transport Properties REFPROP - Users's Guide,* Gaithersburg, Maryland: U.S. Department of Commerce, 2013.

[20] W. Angielczyk, Y. Bartosiewicz, D. Butrimowicz e J. Seynhaeve, «1-D Modeling of supersonic carbon dioxide two-phase flow through ejector motive nozzle,» in *International Refrigeration and Air Conditioning Conference*, Purdue University, 2010.

[21] M. Haida, J. Smolka, A. Hafner, M. Palacz, K. Banasiak e A. J. Nowak, «Modified homogeneous relaxation model for the R744 trans-critical flow in a two-phase ejector,» *International Journal of Refrigeration,* vol. 85, pp. 314-333, 2018.

[22] M. Yazdani, A. A. Alahyari e T. Radcliff, «Numerical modeling of two-phase supersonic ejectors for work-recovery applications,» *International Journal of Heat and Mass Transfer,* vol. 55, pp. 5744-5753, 2012.

[23] F. Giacomelli, F. Mazzelli e A. Milazzo, «A novel CFD approach for the computation of R744 flashing nozzles in compressible and metastable conditions,» *Energy,* vol. 162, pp. 1092-1105, 2018.

[24] F. Giacomelli, Numerical Modeling of Supersonic Two-Phase Ejectors Working with Natural Refrigerants, Firenze: Ph.D. Dissertation, University of Florence, 2018.

[25] S. Elbel e P. Hrnjak, «Experimental validation of a prototype ejector designed to reduce throttling losses encountered in transcritical R744 system operation,» *International Journal of Refrigeration,* pp. 411-422, 2008.

[26] V. P. Carey, Liquid-Vapor Phase-Change Phenomena, CRC Press, 2007.

[27] F. Mazzelli, F. Giacomelli e A. Milazzo, «CFD modeling of condensing steam ejectors: Comparison with an experimental test-case,» *International Journal of Thermal Sciences,* vol. 127, pp. 7-18, 2018.

[28] C. E. Brennen, Cavitation and Bubble Dynamics, Oxford University Press, 1995.

[29] H. Staedke, Gas dynamic aspects of two-phase flow, Weinheim : WILEY-VCH Verlag GmbH & Co. KGaA, 2006.

[30] M. Labois e C. Narayanan, «Non-conservative pressure-based compressible formulation for multiphase flows with heat and mass transfer,» in *Proceedings of 9th International Conference on Multiphase Flow*, Firenze, 2016.

[31] R. Span e W. Wagner, «A New Equation of State for Carbon Dioxide Covering the Fluid Region from the Triple-Point Temperature to 1100K at Pressure up to 800MPa,» *J. Phys. Chem,* vol. 25, n. 6, pp. 1509-1595, 1996.

[32] M. De Lorenzo, P. Lafon, M. Di Matteo, M. Pelanti, J. M. Seynhaeve e Y. Bartosiewicz, «Homogeneous two-phase flow models and accurate steam-water table look-up method for fast transient simulations,» *International Journal of Multiphase Flow,* vol. 95, pp. 199-219, 2017.

[33] F. Giacomelli, G. Biferi, F. Mazzelli e A. Milazzo, «CFD modeling of the supersonic condensation inside a steam ejector,» *Energy Procedia,* pp. 1224-1231, 2016.

[34] Y. Fang, M. De Lorenzo, P. Lafon, S. Poncet e Y. Bartosiewicz, «An Accurate and Efficient Look-up Table Equation of State for Two-phase Compressible Flow Simulations of Carbon Dioxide,» *Industrial and Engineering Chemistry Research,* vol. 57, p. 7676–7691, 2018.

[35] M. Palacz, M. Haida, J. Smolka, A. J. Nowak, K. Banasiak e A. Hafner, «HEM and HRM accuracy comparison for the simulation of CO2 expansion in two-phase ejectors for supermarket refrigeration systems,» *Applied Thermal Engineering,* vol. 115, pp. 160-169, 2017.

[36] F. Mazzelli, F. Giacomelli e A. Milazzo, «Numerical Modeling of a Supersonic Steam Ejector for a Heat Powered Refrigeration System,» in *13th IIR Gustav Lorentzen Conference*, Valencia, 2018.

[37] C. E. Brennen, Fundamentals of Multiphase Flows, Pasadena, California: Cambridge University Press, 2005.